Publication Year	2019
Acceptance in OA	2020-12-18T10:01:52Z
Title	Observations of a Fast-expanding and UV-bright Type Ia Supernova SN 2013gs
Authors	Zhang, Tianmeng, Wang, Xiaofeng, Zhao, Xulin, Xu, Dong, REGUITTI, ANDREA, Zhang, Jujia, PASTORELLO, Andrea, TOMASELLA, Lina, OCHNER, PAOLO, TARTAGLIA, LEONARDO, BENETTI, Stefano, TURATTO, Massimo, HARUTYUNYAN, AVET, ELIAS DE LA ROSA, NANCY DEL CARMEN, Huang, Fang, Zhang, Kaicheng, Chen, Juncheng, Jiang, Zhaoji, Ma, Jun, Nie, Jundan, Peng, Xiyan, Zhou, Xu, Zhou, Zhimin, Zou, Hu
Publisher's version (DOI)	10.3847/1538-4357/aafacd
Handle	http://hdl.handle.net/20.500.12386/28987
Journal	THE ASTROPHYSICAL JOURNAL
Volume	872

The Astrophysical Journal, 872:14 (18pp), 2019 February 10 https://doi.org/10.3847/1538-4357/aafacd

Observations of a Fast-expanding and UV-bright Type Ia Supernova SN 2013gs

Tianmeng Zhang[1,2], Xiaofeng Wang[3], Xulin Zhao[4], Dong Xu[5], Andrea Reguitti[6], Jujia Zhang[7,8,9], Andrea Pastorello[10], Lina Tomasella[10], Paolo Ochner[6], Leonardo Tartaglia[11], Stefano Benetti[10], Massimo Turatto[10], Avet Harutyunyan[12], Nancy Elias-Rosa[10], Fang Huang[3,13], Kaicheng Zhang[3], Juncheng Chen[3], Zhaoji Jiang[1], Jun Ma[1,2], Jundan Nie[1], Xiyan Peng[1], Xu Zhou[1], Zhimin Zhou[1], and Hu Zou[1]

[1] Key Laboratory of Optical Astronomy, National Astronomical Observatories, Chinese Academy of Sciences, Beijing 100012, People's Republic of China
zhangtm@nao.cas.cn
[2] School of Astronomy and Space Science, University of Chinese Academy of Sciences, People's Republic of China
[3] Physics Department and Tsinghua Center for Astrophysics (THCA), Tsinghua University, Beijing, 100084, People's Republic of China
[4] School of Science, Tianjin University of Technology, Tianjin, 300384, People's Republic of China
[5] National Astronomical Observatories, Chinese Academy of Sciences, Beijing 100012, People's Republic of China
[6] Dipartimento di Fisica e Astronomia G. Galilei, Universita' di Padova, Vicolo dell'Osservaotio 3, I-35122, Padova, Italy
[7] Yunnan Observatories (YNAO), Chinese Academy of Sciences, Kunming 650216, People's Republic of China
[8] Key Laboratory for the Structure and Evolution of Celestial Objects, Chinese Academy of Sciences, Kunming 650216, People's Republic of China
[9] Center for Astronomical Mega-Science, Chinese Academy of Sciences, 20A Datun Road, Chaoyang District, Beijing, 100012, People's Republic of China
[10] INAF-Osservatorio Astronomico di Padova, Vicolo dell'Osservatorio 5, I-35122, Padova, Italy
[11] Department of Astronomy, Stockholm University, SE-10691 Stockholm, Sweden
[12] INAF-Fundacion Galileo Galilei, Rambla Jose Ana Fernandez Perez 7, E-38712 Brena Baja, Spain
[13] Department of Astronomy, School of Physics and Astronomy, Shanghai Jiao Tong University, Shanghai, 200240, People's Republic of China

Received 2018 April 23; revised 2018 November 26; accepted 2018 December 20; published 2019 February 6

Abstract

In this paper, we present extensive optical and ultraviolet (UV) observations of the type Ia supernova (SN Ia) 2013gs discovered during the Tsinghua-NAOC Transient Survey. The photometric observations in the optical show that the light curves of SN 2013gs are similar to those of normal SNe Ia, with an absolute peak magnitude of $M_B = -19.25 \pm 0.15$ mag and a post-maximum decline rate $\Delta m_{15}(B) = 1.00 \pm 0.05$ mag. *Gehrels Swift* Ultra-Violet/Optical Telescope observations indicate that SN 2013gs shows unusually strong UV emission (especially in the $uvw1$ band) at around the maximum light ($M_{uvw1} \sim -18.9$ mag). The SN is characterized by relatively weak Fe II III absorptions at ~5000 Å in the early spectra and a larger expansion velocity ($v_{\rm Si} \sim 13{,}000\ {\rm km\ s^{-1}}$ around the maximum light) than the normal-velocity SNe Ia. We discuss the relation between the $uvw1 - v$ color and some observables, including Si II velocity, line strength of Si II $\lambda6355$ and Fe II/III lines, and $\Delta m_{15}(B)$. Compared to other fast-expanding SNe Ia, SN 2013gs exhibits Si and Fe absorption lines with similar strength and bluer $uvw1 - v$ color. We briefly discussed the origin of the observed UV dispersion of SNe Ia.

Key words: supernovae: general – supernovae: individual (SN 2013gs)

1. Introduction

Type Ia supernovae (SNe Ia) have been successfully used as excellent distance indicators to measure the expansion history of the universe (Riess et al. 1998; Perlmutter et al. 1999) because of their high luminosities and standardizable properties through empirical relations between their peak luminosity and light/color-curve shapes (e.g., Phillips 1993; Guy et al. 2005; Wang et al. 2005). It is commonly believed that the explosion of an SN Ia arises from a carbon–oxygen white dwarf (WD) in a binary system that reaches the Chandrasekhar mass limit (~1.4 $M_\odot$; Chandrasekhar 1957; Wang & Han 2012; Maoz et al. 2014). However, the nature of the companion star of the exploding WD is still controversial, as it could be a main-sequence star, a red-giant star, a helium star, or another WD. The former three cases correspond to the single degenerate (SD) scenario (Whelan & Iben 1973), while the last one corresponds to the double degenerate (DD) scenario (Iben & Tutukov 1984; Webbink 1984). Recent studies support both SD (Patat et al. 2007; Sternberg et al. 2011; Dilday et al. 2012) and DD scenarios (Edwards et al. 2012; Schaefer et al. 2012; Santander-Garca et al. 2015).

Observations indicate that the majority of SN Ia explosions belong to the spectroscopically normal or "Branch-normal" subclass (Branch et al. 1993), while the others are somewhat peculiar, including the overluminous SN 1991T-like (Filippenko 1997), subluminous SN 1991bg-like (Filippenko et al. 1992), and the outstanding SN 2002cx-like (Li et al. 2003) subclasses. Multiple criteria have been used to subclassify such explosions. Benetti et al. (2005) defined high-velocity-gradient (HVG) and low-velocity-gradient subgroups, based on the differences in the velocity evolution (or gradient). Branch et al. (2006) used the equivalent width (EW) of Si II $\lambda6355$ and Si II $\lambda5972$ absorptions to classify the SNe Ia into four subgroups: core normal, broad line (BL), cool, and shallow silicon subclasses. The latter two subclasses have a large overlap with peculiar SN 91bg-like and 91T-like subclasses, respectively. Using the Si II velocity measured at around the maximum light, Wang et al. (2009a) divided the SNe Ia into the high-velocity (HV) and the normal-velocity (NV) groups. Some subclasses from different categorizations overlap with each other. For example, HV SNe Ia have similar features as HVG and the BL ones. Wang et al. (2013) compare the SN location in their host galaxy and found that HV SNe Ia are found in more luminous host environments than NV SNe Ia, suggesting that they may originate from different progenitor systems.

Ultraviolet (UV) observations play an important role in understanding diversities of SNe Ia, as the UV emission may be sensitive to the progenitor metallicity (e.g., Höflich et al. 1998; Lentz et al. 2000; Timmes et al. 2003; Sauer et al. 2008) and/or

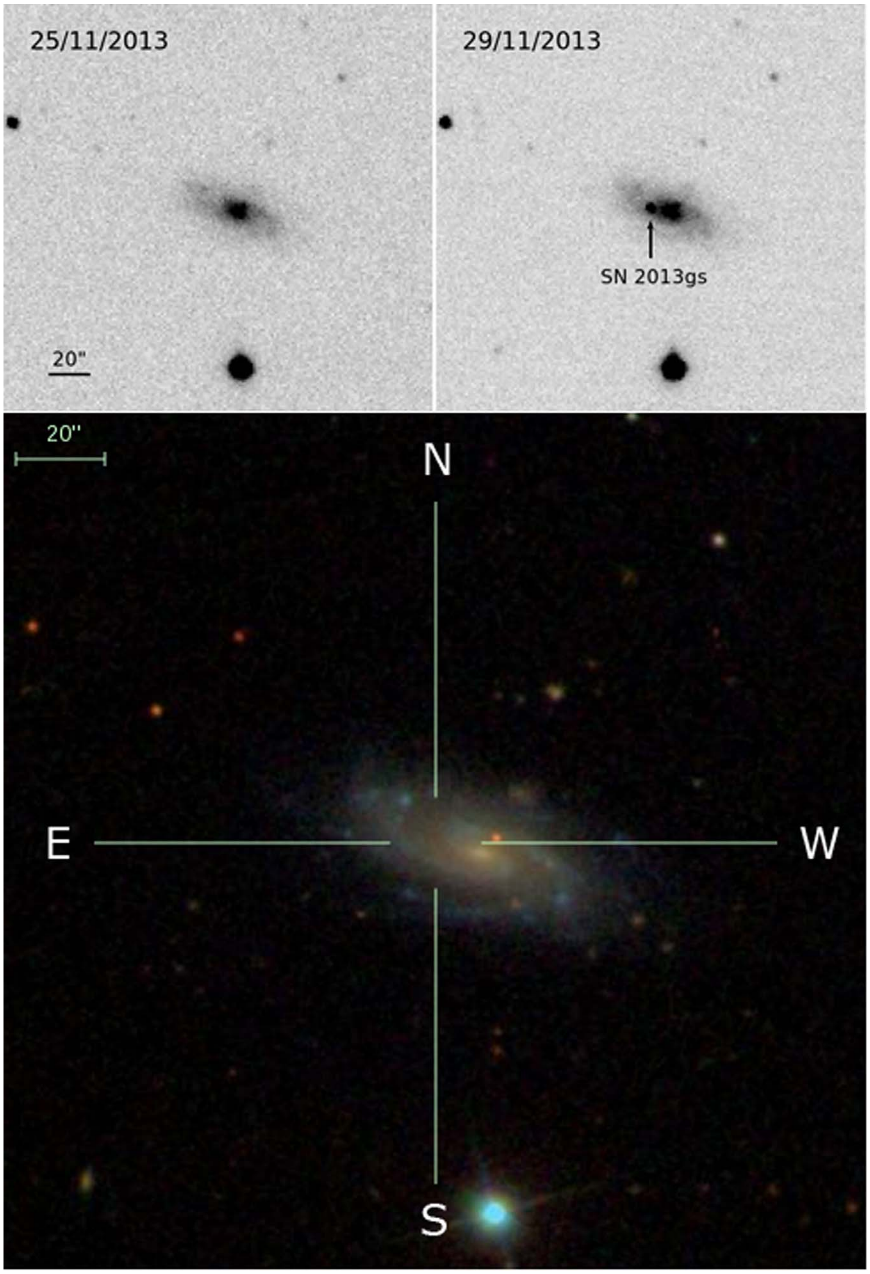

Figure 1. Top left: the unfiltered image without SN 2013gs taken by TNTS on November 24th. Top right: the unfiltered image with SN (marked by the arrow) taken by TNTS on November 29th. Bottom: SDSS color image of the host galaxy of SN 2013gs and the position of SN is marked by the crosshair. North is up and east is to the left.

the interaction of exploding ejecta with the companion star (i.e., Kasen 2010). The UV spectrum of SNe Ia, which is formed in the outer unburned C + O layer, can be attenuated by the absorption lines from the iron-peak elements (Fe II, etc.). However, there is no consensus on the metallicity effect on the UV flux. Based on the pure deflagration model W7 (Nomoto et al. 1984) for SNe Ia, the UV emission increases with decreasing progenitor metallicity (Lentz et al. 2000). Sauer et al. (2008) proposed that the reverse fluorescence scattering of photons from red to blue wavelengths can lead to stronger UV flux with increasing the iron-group elements in the outer layers. Wang et al. (2012) reported that SN 2004dt showed an unusually strong UV excess. This relatively high UV flux could also be used to set constraints on the surrounding circumstellar material (CSM). On the other hand, the UV-optical colors have been used to divide the SNe Ia into several subclasses (Milne et al. 2013), but their scatter is larger than the values predicted by models with various metallicities (Brown et al. 2015). It is thus important to explore the possible origin of the intrinsic dispersion of UV luminosity in SNe Ia. Well-sampled UV observations may help us constrain the properties of progenitor system and the explosion mechanism for the different Type Ia subclasses. Moreover, multiband light curves are also required to accurately estimate the extinction and hence the intrinsic luminosity of SNe Ia.

In this paper, optical/UV photometric and optical spectroscopic observations of SN 2013gs are presented. Observations and data reductions are described in Section 2. Section 3 discusses the light/color curves and the reddening estimate, while Section 4 presents the spectral evolution. We discuss the relationship between the UV flux and some SNe Ia parameters in Section 5.

2. Observations and Data Reduction

SN 2013gs was detected on November 29.84 UT in an unfiltered image taken by the 0.6 m Schmidt telescope in the course of the THU-NAOC Transient Survey (Zhang et al. 2015). The coordinates of this object are $\alpha = 09^{\rm h}31^{\rm m}08\overset{\rm s}{.}87$, $\delta = +46°23'05\overset{''}{.}4$ (J2000.0), located $15\overset{''}{.}0$ east and $2\overset{''}{.}0$ north of the center of an SBbc galaxy UGC 5066 (see Figure 1) with an unfiltered magnitude of about 17.3 mag. Nothing was detected in the image taken on 2013 November 25 UT, with an upper detection limit of ~19.5 mag. A spectrum taken two days after the discovery is consistent with a young SN Ia about 10 days before the maximum (Zhang et al. 2013). The expansion velocity measured from the Si II λ6355 absorption is about 17,500 km $\rm s^{-1}$, which is higher than that of a normal SN Ia at a similar phase.

2.1. Photometry

Our photometric observations of SN 2013gs began on 2013 November 30 (one day after discovery) and lasted for about four months. The optical photometry is mainly obtained with the 0.8 m Tsinghua-NAOC reflecting Telescope (TNT[14]) located at the NAOC Xinglong Observatory. A 1340 × 1300 pixel back-illuminated CCD, with a field of view of $11\overset{'}{.}5 \times 11\overset{'}{.}2$ (pixel size $\sim 0\overset{''}{.}52$ $\rm pixel^{-1}$) is mounted on the Cassegrain focus of the telescope (Huang et al. 2012). Some data were also obtained with the Yunnan Faint Object Spectrograph and Camera (YFOSC) mounted on the Li-Jiang 2.4 m telescope of Yunnan Astronomical Observatories (LJT), the 2.0 m Liverpool Telescope (LT)+IO:O and the Asiago Faint Object Spectrograph & Camera (AFOSC) on the 1.82 m Copernico telescope.[15] The UV observations were triggered immediately after the discovery, with a cadence of 2 days, using the Ultra-Violet/Optical Telescope (UVOT; Roming et al. 2005) on the *Swift* spacecraft (Gehrels et al. 2004). The UV photometry was taken from the Swift Optical/Ultraviolet Supernova Archive[16] (Brown et al. 2014). The reduction is based on that of Brown et al. (2009), including subtraction of the host galaxy count rates and uses the revised UV zero-points and time-dependent sensitivity from Breeveld et al. (2011).

As SN 2013gs is located near the center of UGC 5066, the contamination of the host galaxy cannot be neglected when measuring the SN flux. Therefore, image subtraction was applied before performing photometric measurements with template images taken about one year after the explosion. The SN image is first registered to the template image, and the former is then scaled using the foreground stars to the same point-spread function as the latter. The TNT instrumental magnitudes of the SN and local standard stars are finally obtained with an ad hoc pipeline adapted for the TNT data (based on the IRAF[17] DAOPHOT package; Stetson 1987). The LT and AFOSC data were obtained using a pyhton-based pipeline[18] (Cappellaro et al. 2015).

The *UBVRI* instrumental magnitudes of TNT and YFOSC were transformed to the standard Johnson *UBV* (Johnson et al. 1966) and Kron–Cousins *RI* (Cousins 1981) systems by observing a series of standard stars (Landolt 1992) on photometric nights. The *BV* instrumental magnitudes of LT and AFOSC are calibrated with the Landolt standard stars obtained in eight photometric nights and the *URI* magnitudes are converted from the Sloan catalogs using the relation of Chonis & Gaskell (2008). The calibrated magnitudes of local standard stars are listed in Table 1. The final calibrated magnitude of SN 2013gs is transformed from the instrumental magnitudes by these local standard stars and presented in Table 2. The error bars account for the uncertainties due to photon noise and photometric system calibration.

2.2. Spectroscopy

A total of 22 low-resolution optical spectra were obtained with different telescopes and instruments including the AFOSC on the 1.82 m Copernico telescope, Cassegrain spectrograph and BAO Faint Object Spectrograph and Camera mounted on the 2.16 m telescope at Xinglong Observatory and YFOSC on LJT of Yunnan Astronomical Observatories. The journal of spectroscopic observations is listed in Table 3. In order to reduce the contamination from the host galaxy, the local flux next to SN 2013gs was used as background to carefully extract the SN flux, which was calibrated with standard stars observed on the same night at similar air masses as the SN. The spectra were corrected for the atmospheric extinction using the extinction curves of local observatories, and telluric lines were removed using spectra of standard stars.

3. Light Curves of SN 2013gs

3.1. Optical Light Curves from Ground-based Telescopes

The *UBVRI*-band light curves of SN 2013gs are shown in Figure 2. These multiband observations were used to derive the light-curve parameters such as peak magnitudes and the luminosity decline rate $\Delta m_{15}(B)$. From the polynomial fit, we find that SN 2013gs reached the *B*-band maximum on JD 2,456,640.2 ± 0.2 (2013 December 13.7 UT) with $B_{\rm max} = 15.53 \pm 0.02$ mag and the post-maximum decline rate $\Delta m_{15}(B) = 1.00 \pm 0.05$ mag. From the *B*- and *V*-band light curves, we derived $B_{\rm max} - V_{\rm max} = 0.17 \pm 0.03$ mag, which suggests a non-negligible reddening in the direction of SN 2013gs.

The unfiltered light curve obtained by the 0.6 m Schmidt telescope is also reported in Figure 2 and the magnitudes are listed in Table 3. The unfiltered magnitude was calibrated by the *R*-band magnitude from the Positions and Proper Motions Star Catalog Extended (Röser et al. 2008). The large error bars are mainly attributed to the systematic errors between the unfiltered and *R*-band magnitudes (Li et al. 2003). The unfiltered light curves reached a peak of 15.01 ± 0.20 mag on JD 2,456,641.7 ± 1.2, about 1.5 days after $B_{\rm max}$, while the time of first light will be estimated in Section 3.4.

In Figure 3, we compared the optical light curves of SN 2013gs with other SNe Ia consistent with the SN sample used in the UV comparison, including SNe 2002bo ($\Delta m_{15}(B) = 1.15$;

---

[14] This telescope is co-operated by Tsinghua University and the National Astronomical Observatories of China (NAOC).

[15] This telescope is operated by INAF Osservatorio Astronomico di Padova at Asiago, Italy.

[16] http://swift.gsfc.nasa.gov/docs/swift/sne/swift_sn.html

[17] IRAF, the Image Reduction and Analysis Facility, is distributed by the National Optical Astronomy Observatories, which are operated by the Association of Universities for Research in Astronomy (AURA), Inc., under cooperative agreement with the National Science Foundation.

[18] http://sngroup.oapd.inaf.it/foscgui.html

Table 1

Magnitudes of the Photometric Standards in the Field of SN 2013gs

Star	α	β	U	B	V	R	I	u	g	r	i	z
1	09:30:42.094	46:24:20.27	18.381(026)	17.234(009)	15.977(010)	15.160(046)	14.486(093)	19.256(034)	16.605(011)	15.467(007)	14.993(010)	14.783(003)
2	09:30:43.044	46:18:29.37	18.956(036)	17.960(015)	16.861(014)	16.173(046)	15.501(092)	19.742(047)	17.413(020)	16.415(007)	15.975(011)	15.783(008)
3	09:30:45.212	46:19:46.45	15.693(009)	15.313(008)	14.509(009)	14.071(028)	13.668(054)	16.553(009)	14.867(009)	14.291(007)	14.089(007)	14.047(005)
4	09:30:46.963	46:22:56.27	16.865(013)	16.602(005)	15.831(006)	15.396(028)	14.992(054)	17.731(015)	16.154(009)	15.606(006)	15.401(007)	15.350(003)
5	09:30:54.447	46:25:45.57	15.955(010)	16.154(003)	15.393(004)	14.942(025)	14.668(048)	16.872(004)	15.602(009)	15.201(007)	15.032(007)	15.024(004)
6	09:30:56.043	46:25:07.16	17.985(021)	17.899(019)	17.115(007)	16.645(030)	16.207(058)	18.842(005)	17.455(007)	16.905(006)	16.639(005)	16.578(007)
7	09:30:57.038	46:18:26.44	16.367(011)	16.273(008)	15.381(005)	14.913(027)	14.607(052)	17.269(011)	15.678(007)	15.141(003)	14.959(006)	14.927(004)
8	09:31:14.747	46:18:28.56	15.845(010)	16.016(008)	15.204(006)	14.727(028)	14.396(055)	⋯	15.449(008)	14.987(006)	14.790(011)	14.707(005)
9	09:31:19.112	46:23:47.93	19.149(041)	18.100(010)	16.892(012)	16.086(045)	15.418(092)	⋯	17.509(006)	16.390(003)	15.896(007)	15.697(005)
10	09:31:20.539	46:25:37.45	18.080(022)	17.723(018)	16.893(014)	16.342(034)	15.837(067)	18.932(013)	17.248(007)	16.592(004)	16.289(003)	16.178(007)
11	09:31:28.841	46:26:48.42	18.557(028)	18.383(015)	17.610(022)	17.161(028)	16.756(054)	19.383(039)	17.904(005)	17.402(011)	17.165(005)	17.091(006)
12	09:31:29.905	46:26:42.18	17.083(014)	16.864(007)	16.078(010)	15.630(028)	15.221(054)	⋯	16.399(015)	15.866(006)	15.649(007)	15.575(010)
13	09:31:33.118	46:28:01.39	17.516(016)	16.565(007)	15.421(007)	14.642(044)	13.986(090)	18.424(026)	15.982(010)	14.935(006)	14.484(006)	14.269(007)
14	09:31:37.658	46:26:04.88	20.590(120)	19.521(022)	18.003(012)	17.034(061)	16.169(124)	⋯	18.723(017)	17.417(012)	16.716(008)	16.405(011)
15	09:31:38.263	46:25:13.13	18.784(032)	18.171(020)	17.265(005)	16.664(033)	16.176(065)	⋯	17.677(011)	16.939(008)	16.613(002)	16.494(010)

Table 2
Optical Photometric Observations of SN 2013gs by Ground-based Telescopes

UT Date	MJD	Phase[a]	*U*	*B*	*V*	*R*	*I*	*u*	*g*	*r*	*i*	*z*	Telescope
2013 Nov 30	56626.86	−12.8	17.580(047)	17.523(042)	17.326(035)	17.308(036)	17.135(037)	⋯	⋯	⋯	⋯	⋯	TNT
2013 Dec 1	56627.86	−11.8	17.079(036)	17.126(036)	17.004(037)	16.996(034)	16.856(036)	⋯	⋯	⋯	⋯	⋯	TNT
2013 Dec 2	56628.81	−10.9	⋯	16.756(036)	16.687(034)	16.582(032)	16.525(035)	⋯	⋯	⋯	⋯	⋯	TNT
2013 Dec 3	56629.69	−10.0	⋯	16.553(036)	16.469(037)	16.422(032)	16.305(033)	⋯	⋯	⋯	⋯	⋯	TNT
2013 Dec 5	56631.23	−8.5	⋯	16.226(121)	16.282(070)	16.000(115)	16.105(072)	⋯	⋯	⋯	⋯	⋯	Copernico
2013 Dec 5	56631.80	−7.9	15.776(024)	16.076(034)	16.010(031)	15.922(032)	15.854(033)	⋯	⋯	⋯	⋯	⋯	TNT
2013 Dec 5	56632.15	−7.5	16.022(102)	15.991(066)	16.215(104)	15.993(067)	16.075(100)	⋯	⋯	⋯	⋯	⋯	Copernico
2013 Dec 6	56632.77	−6.9	15.597(059)	15.965(034)	15.915(030)	15.754(031)	15.709(030)	⋯	⋯	⋯	⋯	⋯	TNT
2013 Dec 7	56633.17	−6.5	15.754(101)	15.817(053)	15.954(054)	15.725(049)	15.792(048)	⋯	⋯	⋯	⋯	⋯	Copernico
2013 Dec 8	56634.16	−5.5	15.403(052)	15.772(074)	15.809(077)	15.625(041)	15.715(056)	⋯	⋯	⋯	⋯	⋯	Copernico
2013 Dec 8	56634.80	−4.9	15.495(020)	15.727(034)	15.645(029)	15.576(029)	15.527(029)	⋯	⋯	⋯	⋯	⋯	TNT
2013 Dec 9	56635.04	−3.1	⋯	15.692(044)	15.565(046)	⋯	⋯	⋯	15.544(063)	15.609(040)	⋯	⋯	LT
2013 Dec 9	56635.83	−3.9	15.401(046)	15.618(043)	15.521(038)	15.477(034)	15.474(033)	⋯	⋯	⋯	⋯	⋯	TNT
2013 Dec 10	56636.87	−2.8	15.371(018)	15.589(034)	15.471(032)	15.443(029)	15.502(031)	⋯	⋯	⋯	⋯	⋯	TNT
2013 Dec 11	56637.15	−2.6	15.601(066)	15.735(069)	15.637(053)	15.430(058)	15.850(079)	⋯	⋯	⋯	⋯	⋯	Copernico
2013 Dec 11	56637.85	−1.9	15.366(022)	15.544(032)	15.417(033)	15.387(030)	15.507(033)	⋯	⋯	⋯	⋯	⋯	TNT
2013 Dec 11	56637.96	−1.7	15.600(050)	15.631(043)	15.498(039)	15.450(048)	15.634(065)	⋯	⋯	⋯	⋯	⋯	Copernico
2013 Dec 11	56639.05	−0.7	15.134(067)	15.608(057)	15.667(111)	15.498(115)	15.785(192)	⋯	⋯	⋯	⋯	⋯	Copernico
2013 Dec 13	56639.82	0.1	15.423(023)	15.537(032)	15.365(029)	15.326(031)	15.519(033)	⋯	⋯	⋯	⋯	⋯	TNT
2013 Dec 14	56640.81	1.1	15.429(029)	15.573(035)	15.365(033)	15.322(029)	15.555(036)	⋯	⋯	⋯	⋯	⋯	TNT
2013 Dec 15	56641.87	2.2	15.437(070)	15.593(032)	15.374(033)	15.315(031)	15.578(033)	⋯	⋯	⋯	⋯	⋯	TNT
2013 Dec 17	56643.18	3.4	⋯	15.628(020)	15.389(027)	⋯	⋯	16.517(027)	15.407(021)	15.344(019)	16.001(027)	16.051(022)	LT
2013 Dec 17	56643.84	4.1	⋯	15.689(031)	15.379(010)	15.321(028)	15.636(029)	⋯	⋯	⋯	⋯	⋯	TNT
2013 Dec 18	56644.25	4.6	⋯	15.684(009)	15.426(009)	⋯	⋯	16.663(016)	15.454(010)	15.385(009)	16.078(008)	16.108(010)	LT
2013 Dec 18	56644.70	5.0	⋯	15.703(033)	15.393(028)	15.374(030)	15.705(032)	⋯	⋯	⋯	⋯	⋯	TNT
2013 Dec 19	56645.27	5.6	⋯	15.716(020)	15.422(009)	⋯	⋯	16.734(028)	15.522(012)	15.396(015)	16.111(012)	16.140(009)	LT
2013 Dec 19	56645.84	6.1	15.775(025)	15.761(031)	15.442(030)	15.391(031)	15.720(033)	⋯	⋯	⋯	⋯	⋯	TNT
2013 Dec 20	56646.29	6.6	⋯	15.806(019)	15.466(010)	⋯	⋯	16.872(017)	15.635(015)	15.453(008)	16.139(009)	16.224(011)	LT
2013 Dec 20	56646.87	7.2	⋯	15.839(030)	15.547(030)	15.503(031)	15.830(034)	⋯	⋯	⋯	⋯	⋯	TNT
2013 Dec 21	56647.86	8.2	15.865(094)	15.944(032)	15.590(032)	15.565(032)	15.894(035)	⋯	⋯	⋯	⋯	⋯	TNT
2013 Dec 22	56648.00	8.3	⋯	15.881(053)	15.517(064)	⋯	⋯	17.044(074)	15.757(038)	15.626(046)	16.277(064)	16.303(046)	LT
2013 Dec 22	56648.87	9.2	⋯	15.995(032)	15.635(032)	15.637(032)	15.955(034)	⋯	⋯	⋯	⋯	⋯	TNT
2013 Dec 23	56649.02	9.3	⋯	15.983(020)	15.592(039)	⋯	⋯	17.121(036)	15.807(032)	15.635(028)	16.364(026)	16.336(031)	LT
2013 Dec 23	56649.86	10.2	16.078(053)	16.097(032)	15.709(030)	15.743(031)	16.031(033)	⋯	⋯	⋯	⋯	⋯	TNT
2013 Dec 24	56650.03	10.3	⋯	16.078(032)	15.638(024)	⋯	⋯	17.249(030)	15.737(025)	15.730(024)	16.466(029)	16.373(020)	LT
2013 Dec 25	56651.05	11.4	⋯	16.193(014)	15.709(031)	⋯	⋯	17.349(030)	15.809(016)	15.772(023)	16.524(024)	16.372(030)	LT
2013 Dec 25	56651.89	12.2	16.365(031)	16.260(032)	15.745(031)	15.834(031)	16.079(036)	⋯	⋯	⋯	⋯	⋯	TNT
2013 Dec 26	56652.07	12.4	⋯	16.341(033)	15.777(030)	⋯	⋯	17.448(029)	15.855(023)	15.839(033)	16.586(036)	16.404(043)	LT
2013 Dec 26	56652.81	13.1	16.492(032)	16.330(034)	15.814(030)	15.901(032)	16.123(037)	⋯	⋯	⋯	⋯	⋯	TNT
2013 Dec 27	56653.09	13.4	⋯	16.384(009)	15.806(008)	⋯	⋯	17.648(025)	15.939(009)	15.880(009)	16.644(017)	16.393(011)	LT
2013 Dec 27	56653.69	14.0	16.563(060)	16.408(039)	15.850(033)	15.957(035)	16.190(038)	⋯	⋯	⋯	⋯	⋯	TNT
2013 Dec 28	56654.73	15.0	16.819(035)	16.552(035)	15.978(031)	16.019(032)	16.159(036)	⋯	⋯	⋯	⋯	⋯	TNT
2013 Dec 31	56657.86	18.2	17.111(044)	16.839(040)	16.167(034)	16.133(035)	16.075(037)	⋯	⋯	⋯	⋯	⋯	TNT
2014 Jan 1	56658.87	19.2	17.249(050)	16.922(042)	16.214(035)	16.139(035)	15.999(038)	⋯	⋯	⋯	⋯	⋯	TNT
2014 Jan 4	56661.86	22.2	17.616(068)	17.245(046)	16.353(037)	16.164(037)	16.014(036)	⋯	⋯	⋯	⋯	⋯	TNT
2014 Jan 7	56664.97	25.3	18.137(183)	17.835(120)	16.494(044)	16.140(060)	15.923(077)	⋯	⋯	⋯	⋯	⋯	Copernico
2014 Jan 8	56664.94	26.3	⋯	18.104(154)	16.591(101)	16.436(108)	16.077(151)	⋯	⋯	⋯	⋯	⋯	Copernico
2014 Jan 10	56667.86	28.2	18.063(054)	17.669(030)	16.659(026)	16.261(026)	16.011(027)	⋯	⋯	⋯	⋯	⋯	LJT

Table 2
(Continued)

UT Date	MJD	Phase[a]	U	B	V	R	I	u	g	r	i	z	Telescope
2014 Jan 11	56668.96	29.3	⋯	18.031(074)	16.583(034)	⋯	⋯	19.209(137)	17.350(045)	16.278(029)	16.401(020)	16.225(031)	LT
2014 Jan 13	56670.95	30.3	⋯	18.180(030)	16.752(011)	⋯	⋯	19.228(126)	17.599(018)	16.380(020)	16.507(008)	16.387(012)	LT
2014 Jan 17	56674.59	34.9	⋯	⋯	17.138(041)	16.751(039)	16.240(035)	⋯	⋯	⋯	⋯	⋯	TNT
2014 Jan 21	56678.79	39.1	⋯	18.412(043)	17.309(042)	16.997(039)	16.593(038)	⋯	⋯	⋯	⋯	⋯	TNT
2014 Jan 26	56683.05	43.4	⋯	18.548(136)	17.472(086)	17.054(051)	16.845(043)	⋯	⋯	⋯	⋯	⋯	Copernico
2014 Jan 26	56683.98	44.3	⋯	18.507(019)	17.406(023)	⋯	⋯	20.072(064)	18.118(025)	17.083(023)	17.304(022)	17.168(020)	LT
2014 Jan 27	56684.66	45.0	⋯	18.648(045)	17.548(045)	17.115(041)	16.874(041)	⋯	⋯	⋯	⋯	⋯	TNT
2014 Jan 28	56685.02	45.3	⋯	18.581(013)	17.449(009)	⋯	⋯	20.005(051)	18.147(010)	17.149(008)	17.377(010)	17.209(012)	LT
2014 Feb 2	56691.85	52.1	18.957(061)	18.760(035)	17.892(034)	17.461(032)	17.186(036)	⋯	⋯	⋯	⋯	⋯	LJT
2014 Feb 7	56695.05	55.4	⋯	18.745(023)	17.724(021)	⋯	⋯	20.166(041)	18.271(029)	17.457(022)	17.773(031)	17.756(026)	LT
2014 Feb 9	56697.65	57.9	⋯	18.867(124)	18.028(058)	17.670(064)	17.468(070)	⋯	⋯	⋯	⋯	⋯	TNT
2014 Feb 12	56700.94	61.2	⋯	18.690(037)	17.856(015)	⋯	⋯	20.069(112)	18.279(030)	17.571(015)	17.984(015)	18.034(026)	LT
2014 Feb 27	56715.52	75.8	⋯	19.078(065)	18.422(056)	18.147(035)	18.166(046)	⋯	⋯	⋯	⋯	⋯	TNT
2014 Feb 28	56716.05	76.4	⋯	18.954(029)	18.270(020)	⋯	⋯	20.579(082)	18.523(020)	18.096(026)	18.563(030)	18.771(045)	LT
2014 Mar 1	56717.52	77.8	⋯	19.084(105)	18.452(048)	18.176(030)	18.230(044)	⋯	⋯	⋯	⋯	⋯	TNT
2014 Mar 9	56725.09	85.4	⋯	19.428(162)	18.603(073)	18.403(067)	18.608(072)	⋯	⋯	⋯	⋯	⋯	Copernico
2014 Apr 2	56749.52	109.8	⋯	19.578(150)	19.305(120)	19.328(110)	19.707(120)	⋯	⋯	⋯	⋯	⋯	LJT

Note.
[a] Relative to the epoch of B-band maximum (JD = 2,456,640.2).

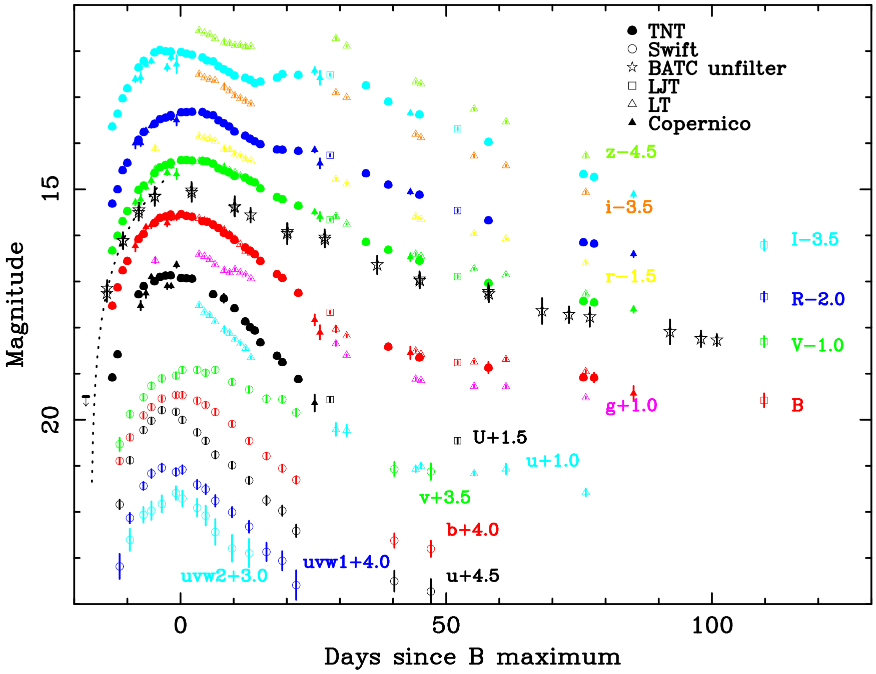

Figure 2. UV and optical light curves of SN 2013gs. The two UV (*uvw*1 and *uvw*2) and three optical (*u*, *b*, and *v*) light curves were obtained by *Gehrels Swift*-UVOT (open circles). The filled circles are the *UBVRI* light curves obtained by TNT. The data coming from the LJT 2.4 m telescope (open squares), the 2.0 m Liverpool telescope (open triangles), and the 1.82 m Copernico Telescope (filled triangles) are also plotted in the figure. The open pentagons show the unfilter light curves of the 0.6 m Schmidt telescope. The light curves are shifted vertically for clarity. The dashed black line is the $t^{1.47}$ fit for unfilter data before -8 days relative to the *B*-band maximum.

Benetti et al. 2004; Krisciunas et al. 2004), 2006X ($\Delta m_{15}(B) = 1.17$; Wang et al. 2008), 2007gi ($\Delta m_{15}(B) = 1.31$; Zhang et al. 2010), 2009ig ($\Delta m_{15}(B) = 0.89$; Foley et al. 2012), and ASASSN-14lp ($\Delta m_{15}(B) = 0.80$; Shappee et al. 2016), 2003du ($\Delta m_{15}(B) = 1.02$; Stanishev et al. 2007), 2005cf ($\Delta m_{15}(B) = 1.05$; Wang et al. 2009b). The *B*-band light curve of ASASSN-14lp is approximated from the *g*-band magnitude through the relation of Chonis & Gaskell (2008). The first five SNe Ia have higher photospheric velocities and can be put into the HV subclass, while the latter two belong to the Normal subclass. The light curves of the comparison sample are normalized to the peaks of SN 2013gs. One can see that SN 2013gs and the comparison SNe Ia have similar light-curve shapes near the maximum brightness. In the early phase, SN 2013gs seems to have a rising rate similar to that of SN 2003du but slower than those of SN 2002bo, SN 2005cf, and SN 2006X. This is evident in the *UBVI* bands but not in the *R*. In the early nebular phase, the evolution of the light curve becomes more complicated. In the *B* band, the later-time decline rate β was estimated to be 1.39 ± 0.11 mag (100 days)$^{-1}$, which is slightly smaller than those of SN 2003du (1.65 ± 0.02 mag (100 days)$^{-1}$) and SN 2005cf (1.62 ± 0.07) mag (100 days)$^{-1}$ as shown in Figure 3(b). The decay rates in other bands are also calculated and listed in Table 5. Although the *RI*-band light curves of SN 2013gs are similar to the comparison SNe Ia, its second bump/shoulder feature (at around $t \approx 25$ days) is weaker than the comparison SNe Ia (in particular the HV SNe Ia).

Table 3
Unfiltered Photometric Observations of SN 2013gs by 0.6 m Schmidt Telescope

UT Date	MJD	Phase[a]	Magnitude	Error
2013 Nov 29	56625.84	−13.86	17.26	0.18
2013 Nov 29	56625.90	−13.80	17.15	0.18
2013 Dec 2	56628.86	−10.84	16.11	0.18
2013 Dec 2	56628.92	−10.78	16.12	0.18
2013 Dec 5	56631.84	−7.86	15.51	0.17
2013 Dec 5	56631.89	−7.81	15.45	0.16
2013 Dec 8	56634.85	−4.85	15.15	0.21
2013 Dec 8	56634.90	−4.80	15.16	0.16
2013 Dec 15	56641.76	2.06	15.02	0.18
2013 Dec 15	56641.82	2.12	15.07	0.20
2013 Dec 23	56649.85	10.15	15.39	0.18
2013 Dec 23	56649.91	10.21	15.37	0.22
2013 Dec 26	56652.89	13.19	15.56	0.16
2014 Jan 2	56659.78	20.08	15.96	0.23
2014 Jan 2	56659.83	20.13	15.92	0.18
2014 Jan 9	56666.83	27.13	16.04	0.17
2014 Jan 9	56666.88	27.18	16.09	0.17
2014 Jan 19	56676.71	37.01	16.64	0.20
2014 Jan 27	56684.68	44.98	16.95	0.17
2014 Jan 27	56684.73	45.03	16.98	0.17
2014 Feb 9	56697.62	57.92	17.22	0.18
2014 Feb 9	56697.72	58.02	17.27	0.18
2014 Feb 19	56707.74	68.04	17.64	0.28
2014 Feb 24	56712.80	73.10	17.72	0.18
2014 Feb 28	56716.71	77.01	17.77	0.21
2014 Mar 15	56731.80	92.10	18.09	0.27
2014 Mar 21	56737.62	97.98	18.24	0.18
2014 Mar 24	56740.62	100.98	18.27	0.13

Note.
[a] Relative to the epoch of *B*-band maximum (JD = 2,456,640.2).

3.2. *UV Light Curves from* Gehrels Swift-*UVOT*

The UV and optical light curves of SN 2013gs obtained by *Gehrels Swift*-UVOT are also shown in Figure 2 and listed in Table 4. SN 2013gs was not detected in the *uvm*2 band (centered at ∼2200 Å) presumably due to the large reddening

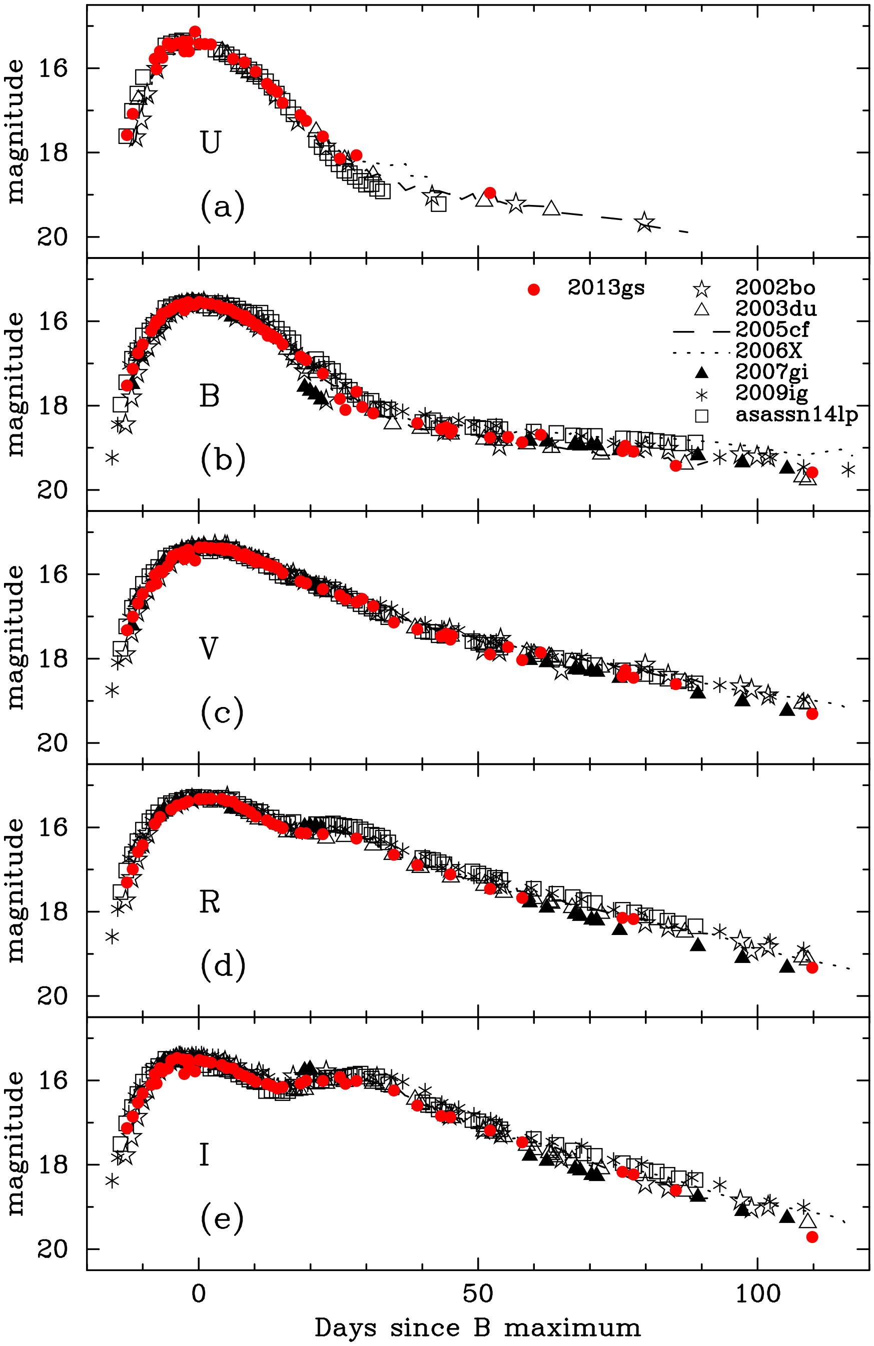

Figure 3. *UBVRI* light curves of SN 2013gs, and the comparison SNe 2002bo, 2003du, 2005cf, 2006X, 2007gi, 2009ig, and ASASSN-14lp (see the text for references). All light curves are shifted in magnitude to match the peak of SN 2013gs.

bump near 2200 Å (Cardelli et al. 1989). In Figure 4, we compared the UV (*uvw*1 and *uvw*2) light curves of SN 2013gs with SN 2005cf ($\Delta m_{15}(B) = 1.05$; Pastorello et al. 2007; Wang et al. 2009b), SN 2006X ($\Delta m_{15}(B) = 1.17$; Brown et al. 2009), SN 2009ig ($\Delta m_{15}(B) = 0.89$; Foley et al. 2012), SN 2011fe ($\Delta m_{15}(B) = 1.18$; Brown et al. 2012b; Zhang et al. 2016), SN 2012fr ($\Delta m_{15}(B) = 0.80$; Zhang et al. 2014; Contreras et al. 2018), and ASASSN-14lp ($\Delta m_{15}(B) = 0.80$; Shappee et al. 2016). The *uvw*1- and *uvw*2-band light curves of SN 2013gs span from $t = -11.5$ days to $t = +6.5$ days relative to the *B*-band maximum. The UV light curves of the comparison SNe Ia have been normalized to their *B*-band maxima and shifted to match the UV peaks of SN 2013gs. The *uvw*1-band light curve of SN 2013gs shows close resemblance to SN 2009ig around the maximum light. In comparison, SN 2006X shows a slower post-maximum decline rate while SN 2011fe declines more rapidly than other SNe Ia. The *uvw*2-band light curve of SN 2013gs is similar to that of SN 2009ig and SN 2011fe, though it has larger photometric errors. The UV light curves of SN 2013gs are similar to those of SN 2009ig. The light-curve parameters of other bands are listed in Table 5.

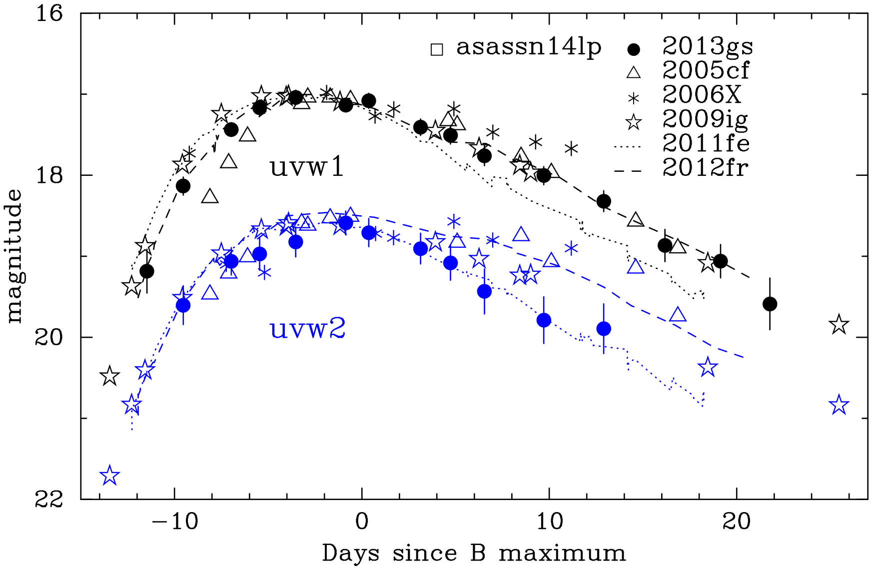

Figure 4. UV light curves of SN 2013gs observed with *Gehrels Swift*-UVOT (*uvw*1 and *uvw*2), compare with SNe 2005cf, 2006X, 2009ig, 2011fe, and 2012fr (see the text for references). All light curves are shifted in magnitude to match the peak of SN 2013gs.

Table 4
Gehrels Swift-UVOT Photometry of SN 2013gs

UT Date	MJD	Phase[a]	*u*	*b*	*v*	*uvw*1	*uvw*2
2013 Dec 2	−11.47	56628.23	17.339(102)	16.894(072)	17.031(143)	19.184(271)	…
2013 Dec 4	−9.53	56630.17	16.380(070)	16.382(062)	16.382(078)	18.135(112)	19.604(239)
2013 Dec 6	−6.97	56632.73	15.723(064)	15.909(058)	16.016(070)	17.437(085)	19.063(169)
2013 Dec 8	−5.46	56634.24	15.520(068)	15.726(060)	15.764(077)	17.168(095)	18.972(201)
2013 Dec 10	−3.53	56636.17	15.294(062)	15.541(055)	15.607(073)	17.041(091)	18.824(184)
2013 Dec 12	−0.86	56638.84	15.329(061)	15.462(053)	15.540(068)	17.135(086)	18.589(147)
2013 Dec 14	0.36	56640.06	15.503(069)	15.466(054)	15.423(070)	17.082(093)	18.709(174)
2013 Dec 16	3.13	56642.83	15.774(071)	15.581(056)	15.419(069)	17.408(102)	18.906(190)
2013 Dec 18	4.73	56644.43	15.957(074)	15.680(058)	15.480(071)	17.508(108)	19.081(215)
2013 Dec 20	6.54	56646.24	16.260(081)	15.836(063)	15.420(071)	17.759(124)	19.434(279)
2013 Dec 23	9.70	56649.40	16.488(074)	16.091(061)	15.682(066)	18.006(112)	19.789(288)
2013 Dec 26	12.90	56652.60	16.817(080)	16.458(064)	15.843(068)	18.321(129)	19.894(307)
2013 Dec 29	16.17	56655.87	17.250(101)	16.791(072)	16.044(078)	18.867(199)	…
2013 Jan 1	19.14	56658.84	17.472(111)	17.056(078)	16.054(078)	19.061(207)	…
2013 Jan 4	21.77	56661.47	17.912(135)	17.307(083)	16.344(085)	19.588(319)	…
2013 Jan 22	40.24	56679.94	19.002(225)	18.622(155)	17.570(153)	…	…
2013 Jan 29	47.16	56686.82	19.225(267)	18.801(175)	17.624(179)	…	…

Note.
[a] Relative to the epoch of *B*-band maximum (JD = 2,456,640.2).

Table 5
Light-curve Parameters of SN 2013gs

Band	$t_{\rm max}$ −2,456,000	$m_{\rm peak}$ (mag)	Δm_{15} (mag)	Δm_{35} (mag)	Δm_{60} (mag)	β[a] mag (100 days)$^{-1}$
unfilter	641.7 ± 1.2	15.01 ± 0.05	0.66 ± 0.22	1.55 ± 0.22	2.43 ± 0.20	2.37 ± 0.07
*uvw*2	639.6 ± 0.4	18.32 ± 0.05	…	…	…	…
*uvw*1	638.6 ± 0.3	16.98 ± 0.04	…	…	…	…
U	640.0 ± 0.3	15.36 ± 0.03	1.46 ± 0.04	…	…	…
B	640.2 ± 0.2	15.53 ± 0.02	1.00 ± 0.05	…	3.35 ± 0.13	1.39 ± 0.17
V	642.1 ± 0.2	15.38 ± 0.02	0.60 ± 0.05	1.76 ± 0.04	2.73 ± 0.06	2.70 ± 0.15
R	640.6 ± 0.2	15.33 ± 0.03	0.67 ± 0.04	1.32 ± 0.04	2.44 ± 0.06	3.34 ± 0.12
I	640.0 ± 0.3	15.49 ± 0.03	0.67 ± 0.05	0.75 ± 0.04	2.07 ± 0.07	4.38 ± 0.08

Note.
[a] The late-time decline rate of light curves.

3.3. The Reddening and Color Curves

The Galactic reddening toward SN 2013gs is $A_V^{\rm Gal} = 0.063$ mag from the dust map of Schlegel et al. (1998) and 0.053 mag from Schlafly & Finkbeiner (2011). We adopted the average value of 0.058 mag, corresponding to $E(B - V) = 0.019$ mag using the standard extinction coefficient $R_V = 3.1$. The reddening from the host galaxy can be estimated through the relation between $\Delta m_{15}(B)$ and $B_{\rm max} - V_{\rm max}$ (see Phillips et al. 1999; Wang et al. 2009b). The comparison gives a host reddening of $E(B - V) = 0.21$ mag for SN 2013gs. With the ΔC_{12} method (Wang et al. 2005), we estimated $E(B - V) = 0.22$ mag. The average value of $E(B - V)_{\rm host} = 0.22 \pm 0.05$ mag is adopted for this paper. The interstellar Na I D doublet lines from the host galaxy are not discerned clearly in the low-resolution spectra of SN 2013gs, hence they cannot be used to estimate independently the host galaxy reddening estimate. The extinction at NUV band varied slightly with different R_V. SN 2013gs is not a very HV Ia like 2006X, so we prefer to use $R_V = 3.1$ to estimate the host galaxy extinction.

Figure 5 presents the reddening-corrected color curves of SN 2013gs. The color curves of SN 2013gs are similar to those of the comparison SNe Ia before and around the maximum light. As shown in Figures 5(a) and (b), SN 2013gs reached its bluest $U - B$ and $B - V$ colors about 7 days before the B-band maximum, while they reach the reddest values about 3–4 weeks after the maximum light. We also note that SN 2002bo, SN 2006X, and SN 2007gi reach their red peaks after maximum about one week earlier than normal SNe Ia (i.e., SN 2003du and SN 2005cf), suggestive of a possible correlation of this difference with ejecta velocity. After $t \sim 1$ months, the color curves of those SNe Ia are characterized by more heterogeneous evolution. In particular, SN 2013gs is bluer than the comparison SNe Ia in $U - B$ and $B - V$, while it is redder in the $V - R$ and $V - I$ colors (Figures 5(c) and (d)). Another interesting feature about SN 2013gs is that its $V - R$ color seems to be bluer than the other SNe Ia at very early phases (i.e., at $t < -10$ days).

The UV color curves of SN 2013gs and the comparison sample are shown in Figure 6. The heterogeneity of the $UV - V$ colors is larger than that of the optical colors, due to the significant change of the photospheric temperature during the explosion and/or a larger line blanketing in the UV domain. The $uvw1 - V$ color curve has sort of a "V" shape, with the bluest color reached about 5 days before the B-band maximum. Such an "V"-shape feature is also mentioned by Milne et al. (2010) and is similarly seen in the $U - B$ and $B - V$ color curves. We note that SN 2013gs has one of the bluest $uvw1 - V$ before the maximum light, similar to SN 2011fe. SN 2011fe also shows very strong UV emission (Zhang et al. 2016) and belongs to the "NUV-blue" group of SNe Ia defined by Milne et al. (2013). In $uvw1 - V$, SN 2013gs is bluer than SN 2009ig by ~0.2–0.4 mag, though these two SNe Ia have similar shapes in their UV light curves. SN 2013gs has the reddest $uvw2 - V$ color among all SNe Ia of our sample for the earliest data point. This deviation may be due to the large uncertainties associated with the red-leak corrections (Brown et al. 2010, 2015). Since SN 2013gs can be associated to both the HV and NUV-blue subclasses of SNe Ia, it apparently becomes an exception for the tendency that NUV-blue events belong to a subset of the larger low-velocity gradient group (Milne et al. 2013).

3.4. The Rise Time

The explosion time of SNe Ia can be inferred from the very early rise of its light curves. Some properties of progenitor systems, such as the radius of the exploding star (Piro & Nakar 2013) or binary interaction (Kasen 2010), can also be constrained by the early time evolution of the light curves. The first detection of SN 2013gs was made at $t = -13.86$ days from the B-band maximum light and an upper limit to ~19.0 mag was found at about $t = -17.80$ days before the B-band maximum. Assuming that SNe Ia expand like homogenous fireballs at very early times, the rise time t_r, depending primarily on the opacity, could be calculated by the t^2 model ($L \propto t^2$; Arnett 1982; Riess et al. 1999). Using the data from the first detection to about 8 days before the B-band maximum and a t^2 model, we constrain the best-fit bolometric rise time as 18.72 ± 0.18 days. This rise time is larger than those of SN 2009ig (17.13 ± 0.07 days; Foley et al. 2012), SN 2011fe (17.64 ± 0.01 days; Zhang et al. 2016), SN 2013dy (~17.8 days; Zheng et al. 2013), ASASSN-14lp (16.94 ± 0.10 days; Shappee et al. 2016), the average Sloan Digital Sky Survey SN Ia (17.38 ± 0.17 days in B band; Hayden et al. 2010), and the average low-redshift SNe Ia (17.44 ± 0.39 days; Strovink 2007). Considering a general form of the fireball model, the index of the power law can be a free parameter ($L \propto t^n$). For the unfiltered light curve as shown in Figure 2, we obtain a best-fit rise time of 16.89 ± 0.88 days and the corresponding index is 1.47 ± 0.26. This smaller index is consistent with the value given by Piro & Nakar (2013) with 1.5. For the model fit with free index, we obtain a rise time of 16.28 ± 1.25 in U, 15.81 ± 0.91 in B, 17.69 ± 1.36 in V, 17.21 ± 3.25 in R, and 18.76 ± 3.03 days in I, respectively. However, the first-light time derived from the above analysis may have great uncertainty due to the lack of early time photometry.

3.5. The Absolute Magnitude and Quasi-bolometric Light Curve of SN 2013gs

The host galaxy of SN 2013gs has a distance modulus of $m - M = 34.29 \pm 0.15$ mag (Mould et al. 2000). Adopting the reddening discussed above, the peak absolute magnitudes of SN 2013gs are $M_U = -19.62 \pm 0.15$ mag, $M_B = -19.29 \pm 0.15$ mag, $M_V = -19.24 \pm 0.15$ mag, $M_R = -19.17 \pm 0.15$ mag, and $M_I = -18.90 \pm 0.15$ mag. They are similar to those of typical SNe Ia (e.g., $M_V = -19.27$ mag from Wang et al. 2006). The UV-band peak absolute magnitudes are also calculated as $M_{uvw1} = -18.86 \pm 0.18$ mag and $M_{uvw2} = -17.87 \pm 0.22$ mag.

We build the quasi-bolometric light curve of SN 2013gs based on the UV and optical photometry to estimate the peak bolometric luminosity and nickel mass produced in the explosion. The bolometric light curves of SN 2013gs are mostly determined by the optical photometry. The early UV contribution is derived from the *Gehrels Swift*-UVOT observations. The ratio between UV (~1500–3000 Å) and optical emission (~3000–9000 Å) is about 0.15 in the rising phase and declined to 0.12 at around the B-band maximum light larger than those of SN 2005cf and SN 2011fe (~10%; Wang et al. 2009b; Zhang et al. 2016) at similar phases. We did not observe SN 2013gs in the near-infrared (NIR) bands, and a contribution of ~5% (derived from SN 2005cf at around the maximum light) is thus applied to the NIR correction of

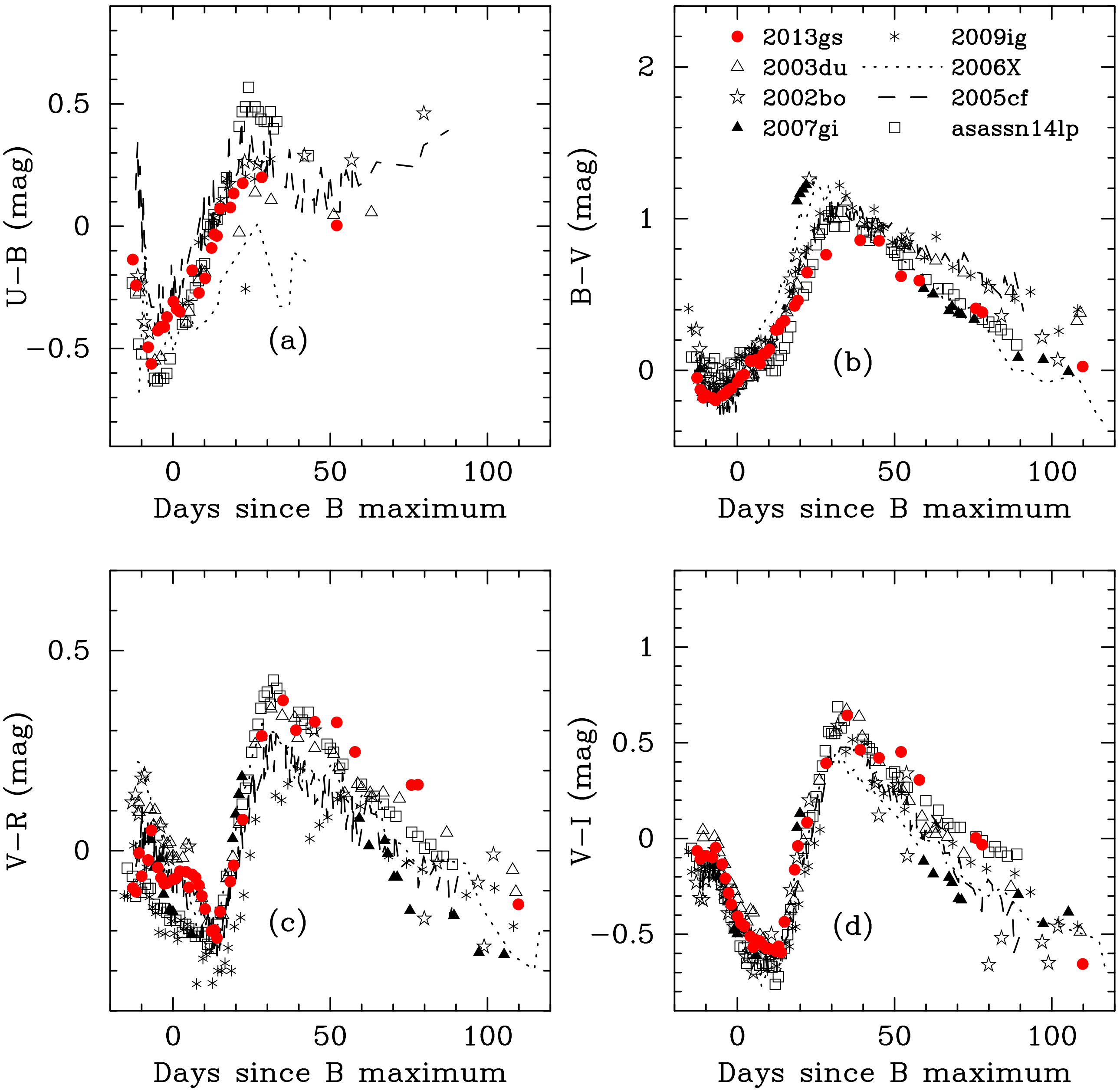

Figure 5. $U-B$, $B-V$, $V-R$, and $V-I$ color curves of SN 2013gs compared with those of SNe 2002bo, 2003du, 2005cf, 2006X, 2007gi, 2009ig, and ASASSN-14lp. All SNe have been dereddened.

bolometric luminosity. For SN 2013gs, the peak bolometric luminosity is estimated to be 1.82 ($\pm$0.16) $\times$ 10^{43} erg s^{-1}, which is comparable to that of other SNe Ia. The error includes uncertainties in distance modulus, photometry, reddening correction, and flux correction beyond the optical window.

Using the Arnett law (Arnett 1982), we can estimate the mass of radioactive ^{56}Ni from the maximum-light luminosity using the following relation:

$$L_{\max} = (6.45 \times e^{\frac{-t_r}{8.8}} + 1.45 \times e^{\frac{-t_r}{111.3}})\, M_{\rm Ni} \times 10^{43}\ {\rm erg\ s^{-1}}, \quad (1)$$

where t_r is the rise time of the bolometric light curve, and $M_{\rm Ni}$ is the mass of ^{56}Ni in unit of solar mass (Stritzinger & Leibundgut 2005). For SN 2013gs, t_r is taken as 16.89 $\pm$ 0.88 days from the analysis in the above subsection. Inserting the parameters of t_r and $L_{\max}$ into the above equation, we derive a nickel mass of 0.83 $\pm$ 0.10 $M_\odot$. This value is within the range of normal SNe Ia.

4. Optical Spectra

A total of 22 optical spectra were taken for SN 2013gs with different telescopes, spanning from $t = -12$ to $+85$ days relative to the B-band maximum. The journal of spectroscopic observations is shown in Table 6. The complete spectral evolution is presented in Figure 7, where the spectra at the maximum brightness are characterized by broad, blueshifted absorption lines of Ca II H and K, Si II λ6355, and the Ca NIR triplet. The detailed spectral evolution is discussed in the following subsections.

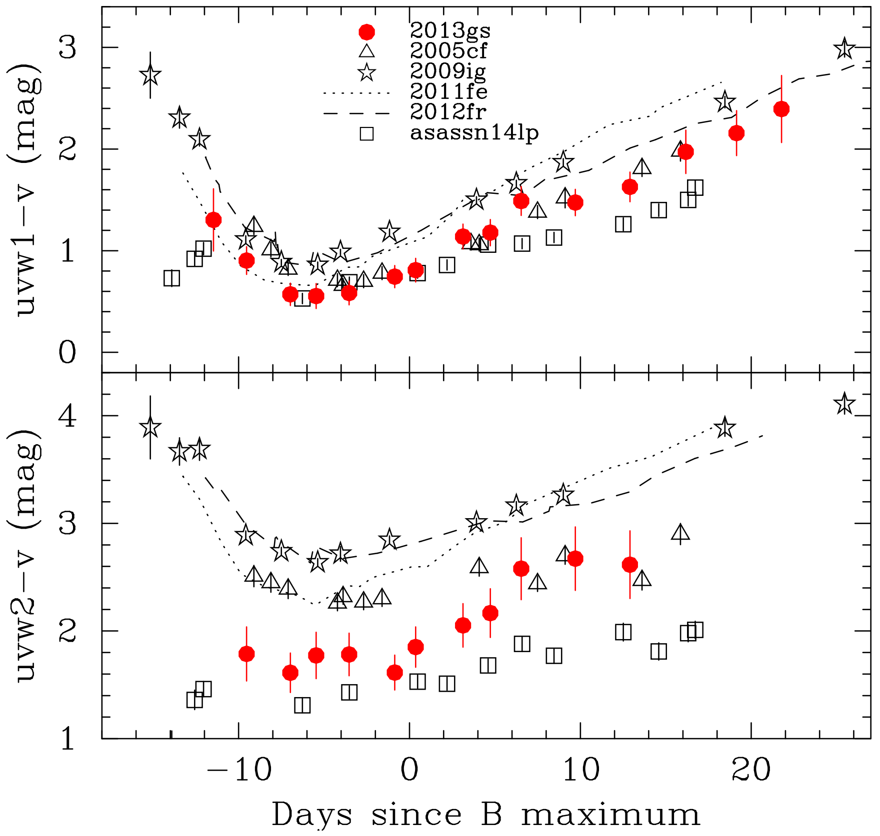

Figure 6. *uvw*1 − *v* and *uvw*2 − *v* colors of SN 2013gs compared with those of SNe 2005cf, 2006X, 2009ig, 2011fe, 2012fr, and ASASSN-14lp (see the text for references). All SNe have been dereddened.

Table 6
Journal of Spectroscopic Observations of SN 2013gs

UT Date	MJD	Phase[a]	Range (Å)	Resolution (Å)[b]	Instrument
2013 Dec 1	56627.3	−12.4	3500–8800	3	YNAO 2.4 m YFOSC
2013 Dec 3	56629.9	−9.8	3800–8700	4	BAO 2.16 m BFOSC
2013 Dec 5	56631.2	−8.5	3700–8200	4	Asiago 1.82 m AFOSC
2013 Dec 6	56632.1	−7.6	3300–10000	5	Asiago 1.82 m AFOSC
2013 Dec 6	56632.8	−6.9	3600–8700	4	BAO 2.16 m BFOSC
2013 Dec 7	56633.1	−6.6	3500–10000	5	Asiago 1.82 m AFOSC
2013 Dec 8	56634.1	−5.6	3300–10000	5	Asiago 1.82 m AFOSC
2013 Dec 9	56635.8	−3.9	3800–8000	4	BAO 2.16 m OMR
2013 Dec 11	56637.1	−2.6	3500–10000	5	Asiago 1.82 m AFOSC
2013 Dec 12	56638.0	−1.7	3500–10000	5	Asiago 1.82 m AFOSC
2013 Dec 13	56639.0	−0.7	3300–10000	5	Asiago 1.82 m AFOSC
2013 Dec 16	56642.4	+2.7	3500–9100	3	YNAO 2.4 m YFOSC
2013 Dec 18	56644.5	+4.8	3200–9200	2	FNT 2.0 m FLOYDS
2013 Dec 27	56653.7	+14.0	3800–8700	4	BAO 2.16 m BFOSC
2013 Dec 27	56653.9	+14.2	3600–10000	5	Asiago 1.82 m AFOSC
2014 Jan 4	56661.7	+22.0	3800–8700	4	BAO 2.16 m BFOSC
2014 Jan 7	56664.9	+25.2	3500–8200	5	Asiago 1.82 m AFOSC
2014 Jan 8	56665.9	+26.2	4700–8200	5	Asiago 1.82 m AFOSC
2014 Jan 25	56683.0	+43.3	3600–10000	5	Asiago 1.82 m AFOSC
2014 Jan 27	56684.7	+45.0	3800–8000	5	BAO 2.16 m BFOSC
2014 Feb 25	56713.1	+73.4	3300–8000	5	Asiago 1.82 m AFOSC
2014 Mar 9	56725.1	+85.4	3700–8200	5	BAO 2.16 m BFOSC

Notes.
[a] Relative to the *V*-band maximum (JD = 2,456,640.2).
[b] Approximate spectral resolution (FWHM intensity).

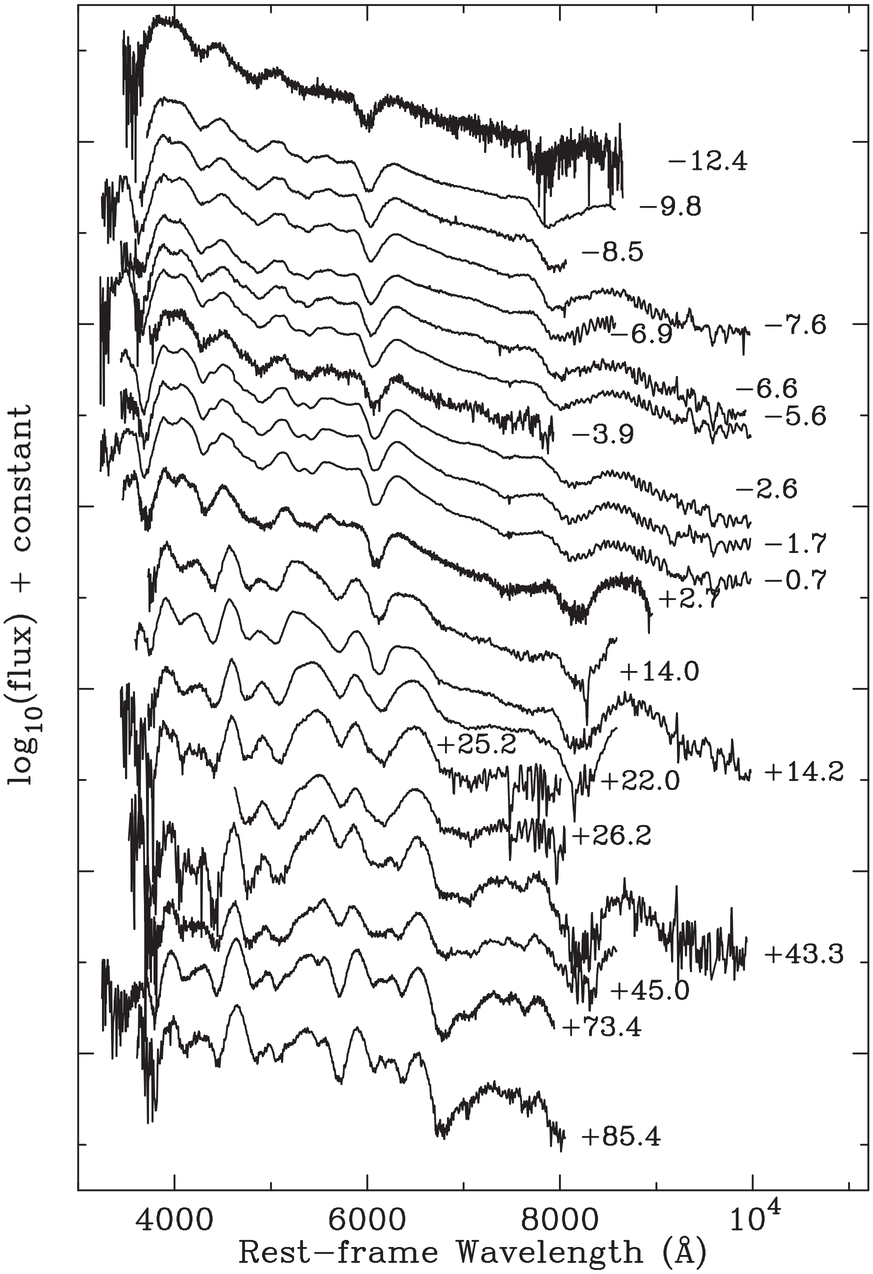

Figure 7. Optical spectral evolution of SN 2013gs. All the spectra have been corrected for the redshift of UGC 05066 ($v_{\mathrm{hel}} = 5063$ km s^{-1}) but only the reddening of Milky Way. The spectra are arbitrarily shifted in the vertical direction for clarity.

4.1. Temporal Evolution of the Spectra

In Figure 8, we compare the spectra of SN 2013gs with well-observed SNe Ia with similar $\Delta m_{15}(B)$ at representative epochs ($t \sim -10$, 0, +1 week and +1 month since the B maximum). The sample includes SN 2002bo (Benetti et al. 2004), SN 2003du (Stanishev et al. 2007), SN 2004dt (Altavilla et al. 2007; Silverman et al. 2012), SN 2005cf (Wang et al. 2009b), and SN 2009ig (Foley et al. 2012). All spectra are corrected for the reddening of the Milky Way and host galaxies.

The earliest spectrum of SN 2013gs taken at $t \approx -12$ days (Figure 8(a)) shows singly ionized lines of intermediate-mass elements like Si, S, Mg, and Ca. The O I λ7773 is not detected in the spectrum of SN 2013gs at any epoch. Compared to other HV SNe Ia, the absorption lines of Si II λ6355 and W-shaped S II features are relatively weak in SN 2013gs. The absorption at about 5800 Å due to Si II λ5972 is barely visible in SN 2013gs, while it is prominent in SNe 2002bo at comparable phases. The Fe II/III absorption (∼5000 Å) is shallower than some HV SNe Ia such as SN 2002bo. SN 2013gs shows a similar Ca NIR triplet to that of SN 2004dt, but the latter has a clear O I absorption, an important spectral diagnostic for constraining the explosion mechanism of SNe Ia (Zhao et al. 2016). At around the maximum brightness (Figure 8(b)), SN 2013gs is quite similar to SN 2002bo, but its spectral features are weaker, especially for the Ca II NIR triplet. We measure R(Si II) (Nugent et al. 1995), the line ratio of Si II λ5972 and Si II λ6355, to be 0.08 ± 0.02 for SN 2013gs. This smaller value of R(Si II) suggests that SN 2013gs has a higher photospheric temperature. It is expected that the spectral energy distribution of SN shifts toward shorter wavelengths with higher photospheric temperatures. The higher temperature

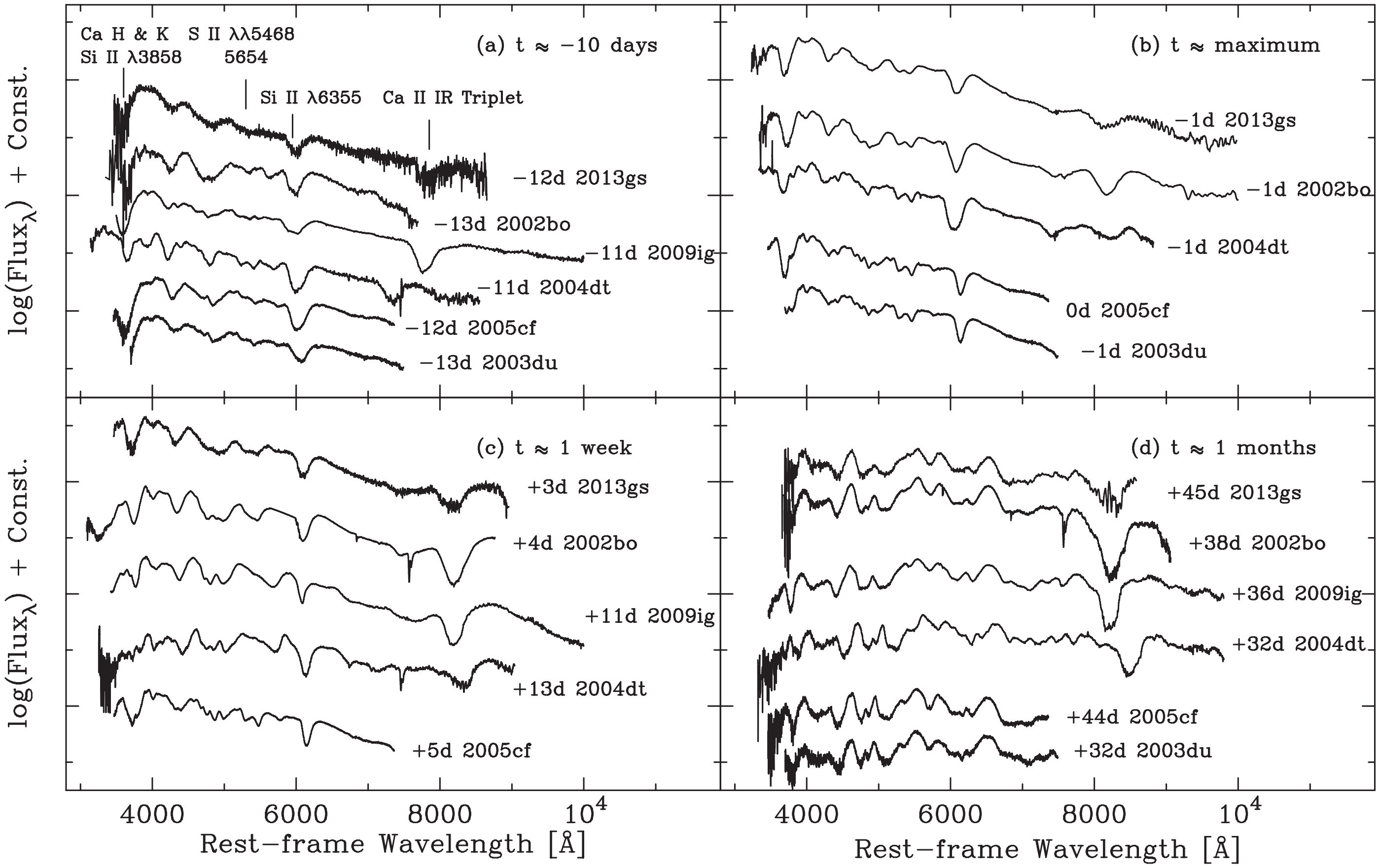

Figure 8. Spectra of SN 2013gs at four different epochs ((a)–(d), $t \approx -12$ days, -1 days, $+3$ days, and 1 months from *B*-band maximum), shown along with spectra of other SNe 2002bo, 2003du, 2004dt, 2005cf, and 2009ig at similar epochs (see the text for references). All spectra have been corrected for the redshift of host galaxy and shifted in the vertical direction for better display.

can also keep the iron-group elements at higher ionization states, which finally results in a lower degree of line blanketing in the UV region (Sauer et al. 2008). This could produce stronger UV emission for SN 2013gs. By one week after maximum light (Figure 8(c)), the W-shaped profile of S II line almost disappeared in SN 2013gs and other HV SNe Ia, while this feature is still visible in SN 2005cf. At $t \sim 1$ month (Figure 8(d)), the spectral profiles of all SNe Ia become quite similar to each other, although the absorptions of the Ca II NIR triplet still shows some diversity in strength.

4.2. Photospheric Expansion Velocity

Figure 9 shows the expansion velocities of SN 2013gs inferred from the Si II 6355 and Ca II NIR triplet absorptions, along with those obtained for SNe 2002bo, 2003du, 2005cf, 2006X, 2007gi, 2009ig, and 2011fe (Silverman et al. 2015; Zhao et al. 2015). The Si II velocity evolution of SN 2013gs is very close to that of SN 2002bo and SN 2009ig, lying between the fast-expanding objects like SN 2006X and the normal SNe Ia like SN 2005cf and SN 2011fe. The profiles of Si II λ6355 from $t = -12$ days to $t = +5$ days are symmetric and can be fitted well with a single-Gaussian function. No HV features are observed in the spectral sequence. Assuming that the expansion velocity of the photosphere decreases in an exponential way, we estimate the Si II velocity of SN 2013gs at peak as $v_{\rm si} = 12{,}800 \pm 400\ {\rm km\ s^{-1}}$ at around the maximum light, with a velocity gradient $\dot{v} = 101 \pm 10\ {\rm km\ s^{-1}}$. These values are noticeably larger than those of normal SNe Ia, putting SN 2013gs into the HV or HVG subclasses of SNe Ia according to the classification schemes proposed by Wang et al. (2009b) and Benetti et al. (2005). The velocities inferred from the S II, and Ca II are higher than Normal SNe Ia by $1000\ {\rm km\ s^{-1}}$, $2000\ {\rm km\ s^{-1}}$, respectively. At $t = -7$ days, the absorption profiles of Ca II H and K are asymmetric, probably as a consequence of contamination from Si II λ3860. It is hard to distinguish the HV component and measure its strength. The absorption line almost keeps a Gaussian profile and varies slowly since $t = -5$ days. The Ca II NIR triplet display a triangle-shaped profile in the spectra of SN 2013gs before $t = -5$ days. The substructures of Ca II λ8498, λ8542, and λ8662 absorptions are blended. In analogy with Si II λ6355 and Ca H and K, the profile of Ca II NIR triplet evolves to become symmetric after $t = -5$ days.

5. Dispersion of the Observed UV Flux

The UV emission of SNe Ia produced in deeper layers are blanketed by the bound–bound transitions from iron-group elements. Thus, most of the UV emission of SNe Ia originates from the outer layers of the ejecta. One of the remarkable characteristics in the spectra of SNe Ia is that the feature of Si II λ6355 is theoretically proposed to vary with the metallicity in the C + O layer. From the synthetic spectra of the W7 model, the increasing metallicity could lead to a blueward shift of the Si II absorption and a decrease in the UV pseudo-continuum (Lentz et al. 2000; Sauer et al. 2008; Walker et al. 2012). We calculate the expansion velocity and pseudo-EW (pEW) of SN

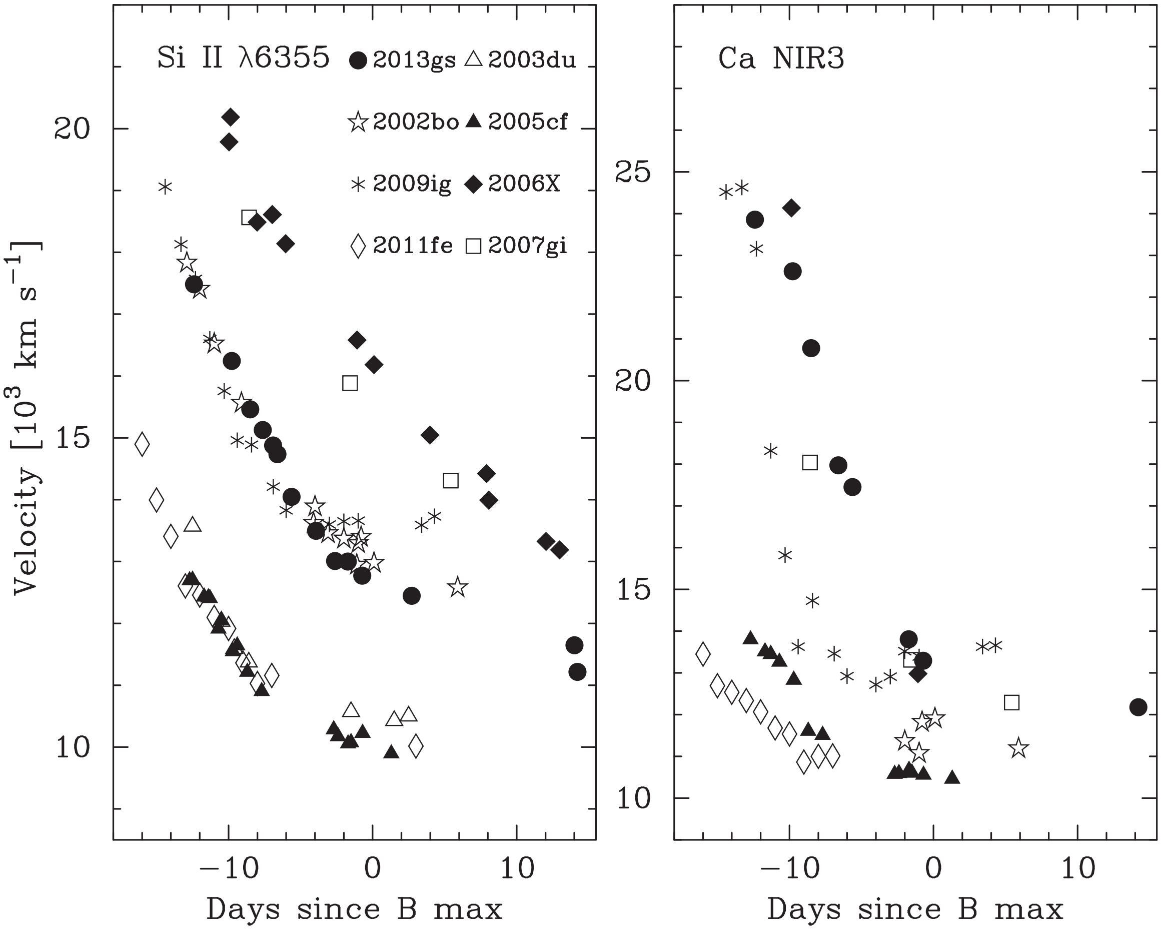

Figure 9. Evolution of the expansion velocity of SN 2013gs measured from the minimum of Si II λ 6355 (left panel) and Ca NIR triplet (right panel) absorptions, compared with those of SNe 2002bo, 2003du, 2005cf, 2006X, 2007gi, 2009ig, and 2011fe (see the text for references).

2013gs at its maximum, and compare with other SNe Ia with different UV-optical color. The UV-optical peak color of comparison SNe Ia mainly come from Brown et al. (2010, 2017). This sample, together with SNe 2004dt[19] (Wang et al. 2012), 2008hv (Brown et al. 2012a), 2009ig (Foley et al. 2012), 2011fe (Brown et al. 2012b), 2012fr (Zhang et al. 2014; Contreras et al. 2018), and ASASSN-14lp (Shappee et al. 2016) from the literature, and 2013gs presented in this paper, are all corrected for their total reddening.

Figure 10 presents the relations between $uvw1 - v$, $b - v$ colors (panel (a)), $\Delta m_{15}(B)$ (panel (b)), Si II velocity (panel (c)), pEW of Si II λ6355 (panel (d)), and Fe II/III (∼5000 Å) absorptions (panel (e)) for these SNe Ia. The colors, velocities, and pEWs are measured around the B-band peak. The velocity of Si II λ6355 ($v_{\rm Si} = 12000$ km s^{-1}) allows us to separate the sample into the HV and NV subclasses. The $uvw1 - v$ and $b - v$ color plots are shown in Figure 10(a). The $(b - v)_{\rm BPEAK}$ of NUV-blue events is bluer than the NUV-red group as mentioned by Milne et al. (2013). In Figure 10(b), we plot the $uvw1 - v$ color versus the B-band post-maximum decline rate $\Delta m_{15}(B)$ for SN 2013gs and some other SNe Ia with UV observations. The HV SNe Ia show a trend that faster decliners have weaker UV fluxes. On the contrary, the $uvw1 - v$ color of NV SNe Ia has a large dispersion and it does not show a correlation between $uvw1 - v$ and $\Delta m_{15}(B)$. Wang et al. (2013) suggested that the progenitors of HV SNe Ia are likely associated with younger and metal-rich stellar environments. Thus the UV emission of SNe Ia may be more sensitive to the metallicity of its progenitors. The different behaviors seen in the observed UV flux of SNe Ia may be related to the difference in their progenitors and explosion models. A recent study by Brown et al. (2017) suggests that SNe Ia with higher ejecta velocities tend to have redder $uvw1 - v$ color. However, SN 2004dt, ASASSN-14lp, and SN 2013gs in our sample do not seem to follow this trend, as shown in Figure 10(c). These outliers provide evidence that the observed UV flux of SNe Ia may be affected by multiple parameters, including metallicity, asymmetric explosions, and circumstellar interaction (Brown et al. 2015). For instance, the shocked ejecta and/or CSM may be compressed into a cool dense shell during the first week after the explosion, which can absorb the X-rays produced by the shock and then reradiate in the UV domain (Fransson 1984, etc.). However, the typical intermediate-width Balmer or helium lines produced by the interaction are not detected in the spectra of these SNe Ia. The asymmetric explosion of SNe Ia will create the inhomogeneities in the ejecta density and structure. Kasen & Plewa (2007) used the detonation from the failed deflagration model to create synthetic spectra observed from different viewing angles. The aspherical distribution of iron-group elements after explosion may also lead a stronger

---

[19] The $uvw1 - v$ colors of SN 2004dt are converted from the *HST* UV photometry.

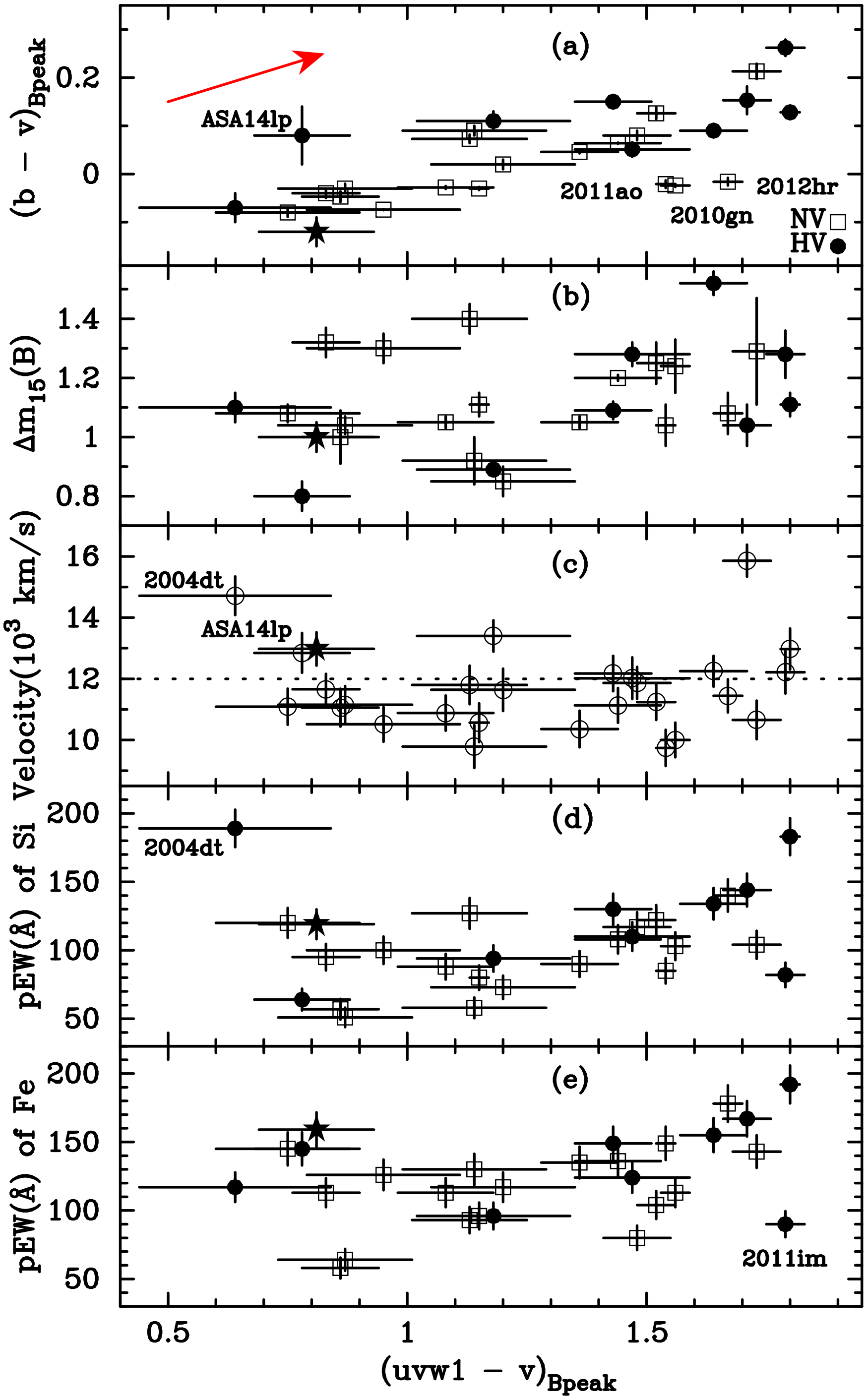

Figure 10. (a): *uvw*1 − *v* vs. *b* − *v* color on maximum light. The sample includes two groups: HV (filled circles) and NV (open squares) Ia. The reddening vector from the Milky Way extinction law (Cardelli et al. 1989) with $E(B-V)=0.1$ is shown by a red arrow; (b): *uvw*1 − *v* vs. $\Delta m_{15}(B)$; (c): *uvw*1 − *v* vs. the velocity of Si II λ6355 around the maximum light, the dotted line ($v_{\rm Si}=12000$ km s^{-1}) in this panel is the boundary between HV and NV Ia; (d): *uvw*1 − *v* vs. pEW of Si II λ6355; (e): *uvw*1 − *v* vs. pEW of Fe II/III (∼5000 Å). The data of SN 2013gs are identified as stars.

flux variation at the UV than the optical bands. In Figures 10(d) and (e), One may see that HV SNe Ia tend to have large pEW of Si II and Fe II/III absorptions relative to the NV ones, as also indicated by previous studies. The trend that lower metallicity results in smaller line velocities was established by Lentz et al. (2000) based on the W7 model. Meanwhile, Lentz et al. (2000) also suggested that the decrease in metallicity leads to increasing UV flux, but with no effects in the optical continuum (Sauer et al. 2008).

6. Summary

In this paper, extensive optical and UV observations are presented for the Type Ia SN 2013gs discovered in UGC 05066 ($z\sim0.0169$) by the Tsinghua-NAOC Transient Survey. The optical photometry started from $t\sim-14$ days before the *B*-band maximum and extended to $t\sim+110$ days. With the unfiltered and multiband light curves, we estimate the peak *B*-band magnitude as $B_{\rm max}=15.53\pm0.02$ mag, $\Delta m_{15}(B)=1.00\pm0.05$ mag, $B_{\rm max}-V_{\rm max}$ color as 0.15 ± 0.03 mag, and a rise time of 16.89 ± 0.88 days. The host galaxy reddening is $E(B-V)=0.22\pm0.05$ mag through several empirical methods, from which we estimate the absolute peak magnitude as $M_B=-19.25\pm0.15$ mag. The overall evolution of the light curve of SN 2013gs is similar to that of SN 2003du.

The UV light curves of SN 2013gs do not match other SNe Ia well, especially at later phases. The reddening-corrected UV colors of SN 2013gs show an excess relative to other HV SNe Ia. This phenomenon is also noticed in another HV SN Ia–SN 2004dt. We estimate the ejected ^{56}Ni mass of $\sim0.8\,M_\odot$ using the quasi-bolometry light curve of SN 2013gs. The spectroscopic behavior of SN 2013gs is consistent with that of typical HV SNe Ia. The Si II absorption velocity $v_{\rm exp}$ is found to be $12{,}800\pm400\ {\rm km\ s^{-1}}$, which indicates that SN 2013gs can be put into the category of HV subclass. The spectral and velocity evolution of SN 2013gs is similar to that of HV SNe Ia like SN 2002bo. The pEW of Si II $\lambda6355$ and Fe II/III (∼5000 Å) measured for SN 2013gs is comparable to that obtained for other HV SNe near the maximum light, but it has bluer $uvw1-V$ colors. Such a strong UV emission is also seen in another two HV Ia SN 2004dt and ASASSN-14lp. This further complicates our understanding of the discrepancy in the UV emission. For the HV SNe Ia, those with slower decline rates ($\Delta m_{15}(B)$) tend to have stronger UV emission, while this tendency does not hold for the sample of NV SNe Ia.

This work is supported by the National Natural Science Foundation of China (NSFC grants 11178003, 11325313, and 11633002), Strategic Priority Research Program of the Chinese Academy of Sciences, grant No. XDB023000000. This work is partially supported by the National Natural Science Foundation of China (NSFC grants 11603034, 11433005 and 11673027) and the External Cooperation Program of Chinese Academy of Sciences (grant No. 114A11KYSB20160057). D.X. acknowledges the supports by the One-Hundred-Talent Program of the Chinese Academy of Sciences (CAS), by the Strategic Priority Research Program "Multi-wavelength Gravitational Wave Universe" of the CAS (No. XDB23000000), and by the National Natural Science Foundation of China under grant 11533003. Funding for the LJT has been provided by the Chinese Academy of Sciences (CAS) and the People's Government of Yunnan Province. The LJT is jointly operated and administrated by Yunnan Observatories and Center for Astronomical Mega-Science, CAS. J.-J.Z. is supported by NSFC (grants 11403096 and 11773067), the Youth Innovation Promotion Association of the CAS, the Western Light Youth Project, and the Key Research Program of the CAS (grant No. KJZD-EW-M06). We acknowledge the support of the staff of the Xinglong 2.16 m/80 cm/Schmidt telescopes. This work was partially supported by the Open Project Program of the Key Laboratory of Optical Astronomy, National Astronomical Observatories, Chinese Academy of Sciences. A.P., L.T., S.B., P.O., and M.T. are partially supported by the PRIN-INAF 2017 toward the SKA and CTA era: discovery, localisation and physics of transient sources (PI M. Giroletti).

ORCID iDs

Tianmeng Zhang https://orcid.org/0000-0002-8531-5161
Xiaofeng Wang https://orcid.org/0000-0002-7334-2357

References

Altavilla, G., Stehle, M., Ruiz-Lapuente, P., et al. 2007, A&A, 475, 585
Arnett, W. D. 1982, ApJ, 253, 785
Benetti, S., Cappellaro, E., Mazzali, P. A., et al. 2005, ApJ, 623, 1011
Benetti, S., Meikle, P., Stehle, M., et al. 2004, MNRAS, 348, 261
Branch, D., Dang, L. C., Hall, N., et al. 2006, PASP, 118, 560
Branch, D., Fisher, A., & Nugent, P. 1993, AJ, 106, 2383
Breeveld, A. A., Landsman, W., Holland, S. T., et al. 2011, AIPC, 1358, 373
Brown, P. J., Baron, E., Milne, P., Roming, P. W. A., & Wang, L. 2015, ApJ, 809, 37
Brown, P. J., Breeveld, A. A., Holland, S., Kuin, P., & Pritchard, T. 2014, Ap&SS, 354, 89
Brown, P. J., Dawson, K. S., de Pasquale, M., et al. 2012b, ApJ, 753, 22
Brown, P. J., Dawson, K. S., Harris, D. W., et al. 2012a, ApJ, 749, 18
Brown, P. J., Holland, S. T., Immler, S., et al. 2009, AJ, 137, 4517
Brown, P. J., Landez, N. J., Milne, P. A., & Stritzinger, M. D. 2017, ApJ, 836, 232
Brown, P. J., Roming, P. W. A., Milne, P., et al. 2010, ApJ, 721, 1608
Cappellaro, E., Botticella, M. T., Pignata, G., et al. 2015, A&A, 584, 62
Cardelli, J. A., Clayton, G. C., & Mathis, J. S. 1989, ApJ, 345, 245
Chandrasekhar, S. 1957, An Introduction to the Study of Stellar Structure (New York: Dover)
Chonis, T. S., & Gaskell, C. M. 2008, AJ, 135, 264
Contreras, C., Phillips, M. M., Burns, C. R., et al. 2018, ApJ, 859, 24
Cousins, A. W. J. 1981, SAAOC, 6, 4
Dilday, B., Howell, D. A., Cenko, S. B., et al. 2012, Sci, 337, 942
Edwards, Z. I., Pagnotta, A., & Schaefer, B. E. 2012, ApJ, 747, 19
Falco, E. E., Kurtz, M. J., Geller, M. J., et al. 1999, PASP, 111, 438
Filippenko, A. V. 1997, ARA&A, 35, 309
Filippenko, A. V., Richmond, M. W., Branch, D., et al. 1992, AJ, 104, 1543
Foley, R. J., Challis, P. J., Filippenko, A. V., et al. 2012, ApJ, 744, 38
Fransson, C. 1984, A&A, 132, 115
Gehrels, N., Chincarini, G., Giommi, P., et al. 2004, ApJ, 611, 1005
Guy, J., Astier, P., Nobili, S., Regnault, N., & Pain, R. 2005, A&A, 443, 781
Hayden, B. T., Garnavich, P. M., Kessler, R., et al. 2010, ApJ, 712, 350
Höflich, P., Wheeler, J. C., & Thielemann, F. K. 1998, ApJ, 495, 617
Huang, F., Li, J., Wang, X., et al. 2012, RAA, 12, 1585
Iben, I., Jr., & Tutukov, A. V. 1984, ApJS, 54, 335
Johnson, H. L., Iriarte, B., Mitchell, R. I., & Wisniewskj, W. Z. 1966, CoLPL, 4, 99
Kasen, D. 2010, ApJ, 708, 1025
Kasen, D., & Plewa, T. 2007, ApJ, 662, 459
Krisciunas, K., Suntzeff, N. B., Phillips, M. M., et al. 2004, AJ, 128, 3034
Landolt, A. U. 1992, AJ, 104, 340
Lentz, E. J., Baron, E., Branch, D., Hauschildt, P. H., & Nugent, P. E. 2000, ApJ, 530, 966
Li, W., Bloom, J. S., Podsiadlowski, P., et al. 2011, Natur, 480, 348
Li, W., Filippenko, A. V., Chornock, R., et al. 2003, PASP, 115, 453
Maoz, D., Mannucci, F., & Nelemans, G. 2014, ARA&A, 52, 107
Milne, P. A., Brown, P. J., Roming, P. W. A., et al. 2010, ApJ, 721, 1627
Milne, P. A., Brown, P. J., Roming, P. W. A., Bufano, F., & Gehrels, N. 2013, ApJ, 779, 23
Mould, J. R., Huchra, J. P., Freedman, W. L., et al. 2000, ApJ, 529, 786
Nomoto, K., Thielemann, F. K., & Yokoi, K. 1984, ApJ, 286, 644
Nugent, P., Phillips, M., Baron, E., Branch, D., & Hauschildt, P. 1995, ApJL, 455, L147
Pastorello, A., Taubenberger, S., Elias-Rosa, N., et al. 2007, MNRAS, 376, 1301
Patat, F., Chandra, P., Chevalier, R., et al. 2007, Sci, 317, 924
Perlmutter, S., Aldering, G., Goldhaber, G., et al. 1999, ApJ, 517, 565
Phillips, M., Lira, R., Suntzeff, N. B., et al. 1999, AJ, 118, 1766
Phillips, M. M. 1993, ApJL, 413, L105
Piro, A., & Nakar, E. 2013, ApJ, 769, 67
Riess, A. G., Filippenko, A. V., Challis, P., et al. 1998, AJ, 116, 1009
Riess, A. G., Filippenko, A. V., Li, W., & Schmidt, B. P. 1999, AJ, 118, 2668
Roming, P. W. A., Kennedy, T. E., Mason, K. O., et al. 2005, SSRv, 120, 95
Röser, S., Schilbach, E., Schwan, H., et al. 2008, A&A, 488, 401
Santander-Garca, M., Rodrguez-Gil, P., Corradi, R. L. M., et al. 2015, Natur, 519, 63
Sauer, D. N., Mazzali, P. A., Blondin, S., et al. 2008, MNRAS, 391, 1605
Schaefer, B. E., & Pagnotta, A. 2012, Natur, 481, 164
Schlafly, E. F., & Finkbeiner, D. P. 2011, ApJ, 737, 103
Schlegel, D. J., Finkbeiner, D. P., & Davis, M. 1998, ApJ, 500, 525

Shappee, B. J., Piro, A. L., Holoien, T. W.-S., et al. 2016, ApJ, 824, 144
Silverman, J. M., Foley, R. J., Filippenko, A. V., et al. 2012, MNRAS, 425, 1789
Silverman, J. M., Vinkó, J., Marion, G. H., et al. 2015, MNRAS, 451, 1973
Stanishev, V., Goobar, A., Benetti, S., et al. 2007, A&A, 469, 645
Sternberg, A., Gal-Yam, A., Simon, J. D., et al. 2011, Sci, 333, 856
Stetson, P. B. 1987, PASP, 99, 191
Stritzinger, M., & Leibundgut, B. 2005, A&A, 431, 423
Strovink, M. 2007, ApJ, 671, 1084
Timmes, F. X., Brown, E. F., & Truran, J. W. 2003, ApJL, 590, L83
Walker, E. S., Hachinger, S., Mazzali, P. A., et al. 2012, MNRAS, 427, 103
Wang, B., & Han, Z. 2012, NewAR, 56, 122
Wang, X., Filippenko, A. V., Ganeshalingam, M., et al. 2009a, ApJL, 699, L139
Wang, X., Li, W., Filippenko, A. V., et al. 2008, ApJ, 675, 626
Wang, X., Li, W., Filippenko, A. V., et al. 2009b, ApJ, 697, 380
Wang, X., Wang, L., Filippenko, A. V., et al. 2012, ApJ, 749, 126
Wang, X., Wang, L., Filippenko, A. V., Zhang, T., & Zhao, X. 2013, Sci, 340, 170
Wang, X., Wang, L., Pain, R., et al. 2006, ApJ, 645, 488
Wang, X., Wang, L., Zhou, X., Lou, Y., & Li, Z. 2005, ApJL, 620, L87
Webbink, R. F. 1984, ApJ, 277, 355
Whelan, J., & Iben, I., Jr. 1973, ApJ, 186, 1007
Zhang, J., Wang, X., Bai, J., et al. 2014, AJ, 148, 1
Zhang, K., Wang, X., Zhang, J., et al. 2016, ApJ, 820, 67
Zhang, T., Wang, X., Chen, J., et al. 2015, RAA, 15, 215
Zhang, T., Wang, X., Li, W., et al. 2010, PASP, 122, 1
Zhang, T., Wang, X., Zhou, L., et al. 2013, CBET, 3734, 1
Zhao, X., Maeda, K., Wang, X., et al. 2016, ApJ, 826, 211
Zhao, X., Wang, X., Maeda, K., et al. 2015, ApJS, 220, 20
Zheng, W., Silverman, J. M., Filippenko, A. V., et al. 2013, ApJL, 778, L15